Monthly Notices
of the
ROYAL ASTRONOMICAL SOCIETY

MNRAS **478,** 4084–4100 (2018) doi:10.1093/mnras/sty1092
Advance Access publication 2018 May 04

MUSE observations of M87: radial gradients for the stellar initial-mass function and the abundance of sodium

Marc Sarzi,[1]★ Chiara Spiniello,[2] Francesco La Barbera,[2] Davor Krajnović[3] and Remco van den Bosch[3]

[1] *Centre for Astrophysics Research, University of Hertfordshire, Hatfield, Herts AL1 9AB, UK*
[2] *INAF-Osservatorio Astronomico di Capodimonte, Salita Moiariello, 16, I-80131 Napoli, Italy*
[3] *Leibniz-Institute fur Astrophysics Potsdam (AIP), An der Sternwarte 16, D-14482 Potsdam, Germany*

Accepted 2018 April 26. Received 2018 April 25; in original form 2017 August 22

ABSTRACT

Based on Multi-Unit Spectroscopic Explorer (MUSE) integral-field data we present evidence for a radial variation at the low-mass end of the stellar initial-mass function (IMF) in the central regions of the giant early-type galaxy NGC 4486 (M87). We used state-of-the-art stellar-population models and the observed strength of various IMF-sensitive absorption-line features to solve for the best low-mass tapered ‘bimodal’ form of the IMF, while accounting also for variations in stellar metallicity, the overall α-elements abundance and the abundance of individual elements such as Ti, O, Na, and Ca. Our analysis reveals a strong negative IMF gradient corresponding to an exceeding fraction of low-mass stars compare(Cappellari & d to the case of the Milky Way towards the centre of M87, which drops to nearly Milky Way levels by 0.4 R_e. Such IMF variations correspond to over a factor 2 increase in stellar mass-to-light M/L ratio compared to the case of a Milky Way IMF, consistent with independent constraints on M/L radial variations in M87 from dynamical models. We also looked into the abundance of sodium in M87, which turned up to be super-Solar over the entire radial range of our MUSE observations and to exhibit a considerable negative gradient. These findings suggest an additional role of metallicity in boosting the Na-yields in the central, metal-rich regions of M87 during its early and brief star formation history. Our work adds M87 to the few objects that presently have radial constraints on their IMF or [Na/Fe] abundance, while also illustrating the accuracy that MUSE could bring to this kind of investigations.

Key words: galaxies: abundances – galaxies: elliptical and lenticular, cD – galaxies: evolution – galaxies: formation.

1 INTRODUCTION

When it comes to painting a comprehensive picture for the formation and evolution of galaxies, one of the key ingredients to consider is the mass distribution with which stars initially form out of their giant cradles of cold, molecular gas. For instance, measuring such an stellar initial-mass function (IMF) in the optical regions of galaxies allows to weigh the relative fraction of stellar and dark matter, which helps in understanding how dark and baryonic matter interact (e.g. Auger et al. 2010; Sonnenfeld et al. 2012). Constraining the IMF of passively evolving stellar systems makes it also possible to reconstruct their luminosity evolution and thus correctly interpret the cosmic evolution of the most massive galaxies in the Universe. Finally – by providing the ratio of high-to-low mass stars – the form of the IMF offers an handle on the amount of energetic feedback that star formation can re-inject in the interstellar medium (ISM) and thus contribute to regulate the formation of galaxies (e.g. Piontek & Steinmetz 2011; Fontanot et al. 2017).

Despite its importance, an exhaustive theory for the origin of the IMF it still lacking, in particular for environments other than the disc of the Milky Way or its globular clusters. In fact, whereas in our immediate galactic neighbourhood there is little evidence for variations in the IMF (see e.g. Bastian, Covey & Meyer 2010), in the last few years a number of studies have claimed a steepening at the low-mass end of the IMF in the most massive galaxies, either from the analysis of integrated spectra (e.g. van Dokkum & Conroy 2010; Conroy & van Dokkum 2012b; Smith, Lucey & Carter 2012; La Barbera et al. 2013; McDermid et al. 2014; Spiniello et al. 2014; Spiniello, Trager & Koopmans 2015b), gravitational lensing (e.g. Treu et al. 2010; Spiniello et al. 2012, 2015a; Leier et al. 2016), or modelling of the stellar kinematics (e.g. Thomas et al. 2011b; Cappellari et al. 2012).

★ E-mail: m.sarzi@herts.ac.uk

© 2018 The Author(s)
Published by Oxford University Press on behalf of the Royal Astronomical Society

Downloaded from https://academic.oup.com/mnras/article/478/3/4084/4992755 by Biblioteca di Scienze, Università degli studi di Firenze user on 22 April 2021

Theoretically, one way of obtaining such a bottom-heavy IMF is to consider molecular clouds characterized by supersonic turbulence, which would lead to more fragmentation and to a lower characteristic mass of the IMF (e.g. Padoan & Nordlund 2002; Hopkins 2013; Chabrier, Hennebelle & Charlot 2014). In this picture, such a supersonic turbulence would be driven by a large rate of supernovae (SN) explosions sustained in turn by a high rate of star formation, which would be consistent with the current view whereby most of the stars in massive early-type galaxies (ETGs) formed early-on during very intense star formation episodes (e.g. Thomas et al. 2005). Alternatively, a bottom-heavy IMF could result from a high pressure or metallicity in the ISM, within models where the bulk of the IMF is set by radiation feedback (e.g. Krumholz 2011). Either way, a time-dependent scenario seems to be required in order to match the stellar metallicity and α-element abundance of massive ETGs, where an early and intense star-bursting stage actually characterized by a top-heavy IMF precedes a relatively more prolonged star formation phase with a bottom-heavy IMF (Weidner et al. 2013; Ferreras et al. 2015).

The early findings that the variation towards a bottom-heavy IMF correlates with the overabundance in α-elements observed in the old stars of massive ETGs (Conroy & van Dokkum 2012b; Smith et al. 2012) would support the previous turbulence-driven picture, as indeed such a characteristic [α/Fe] abundance pattern requires short star formation time-scales that go in the direction of driving high star formation rates. On the other hand, other works point towards a strong correlation with stellar velocity dispersion σ for the variation of the IMF (Cappellari et al. 2012; Spiniello et al. 2012, 2014), which is more difficult to interpret, in particular since σ is known to correlate with other global properties of ETGs, such as mass, luminosity, metallicity [Z/H] and [α/Fe] abundance. It is also possible that such a trend with σ indicates an even closer tie with the local depth of the potential well. This would indeed be similar to the case of the global correlation between the Mgb index and σ (Davies, Sadler & Peletier 1993), when Mgb turned out – thanks to integral-field data – to follow more closely the escape velocity $V_{\rm esc}$, both locally and in a similar way across different galaxies (Scott et al. 2009). In fact, the recent finding of a tight correlation between total metallicity and dwarf-to-giant ratio (Martín-Navarro et al. 2015c) could also be consistent with a close link between this ratio and the local depth of the potential well. The Mgb–$V_{\rm esc}$ correlation is indeed predominantly driven by the variation of [Z/H] with $V_{\rm esc}$, in particular in old stellar populations (Scott et al. 2013), so that the trend between metallicity and low-mass end IMF slope may indirectly result from correlations between [Z/H] and $V_{\rm esc}$ and $V_{\rm esc}$ and IMF slope.

At this point it is important to realize that previous IMF findings are for the most part based on large-aperture measurement or global dynamical models where all information internal to those systems is lost. An handful resolved studies have appeared as of today (Martín-Navarro et al. 2015a; La Barbera et al. 2016; Mentz et al. 2016; La Barbera et al. 2017; van Dokkum et al. 2017), and whereas many report the presence of IMF gradients indicating more dwarf-rich stellar populations towards the centre other studies find little or no evidence for radial IMF variations (see e.g. Martín-Navarro et al. 2015b for the special case of the compact ETG NGC1277 and the work of Alton, Smith & Lucey 2017, who also report no evidence for a bottom-heavy IMF throughout their sample), stressing the importance of also accounting for radial gradients in the abundance of elements entering the IMF-sensitive absorption-line features (such the abundance of sodium entering the NaI feature at 0.81 nm, Zieleniewski et al. 2015; McConnell, Lu & Mann 2016).

Stepping in this direction, in this paper we present high-quality integral-field spectroscopic observations of the giant elliptical NGC 4486 (M87) obtained with the Multi-Unit Spectroscopic Explorer (MUSE, Bacon et al. 2010) on the Very Large Telescope during the first Science Verification observing run for this instrument. Using the unique wavelength coverage and sensitivity of MUSE, we extract high-quality aperture spectra and combine the analysis of dwarf-sensitive features such as those defined in La Barbera et al. (2013) and Spiniello et al. (2014) with constraints on the stellar age, metallicity and [α/Fe], as well as individual abundance ratios, based on standard optical absorption-line indices (Trager et al. 1998; Cenarro et al. 2001). This allows us to set firm constraints on the IMF as a function of radius, which we compare to radial variations for the stellar age, metallicity, [α/Fe] abundance, and stellar velocity dispersion. In the process we also explore the need for a radial variation of the [Na/Fe] abundance, which could provide insights on the yields of odd-numbered elements in high-metallicity and alpha-enhanced stellar populations, such as those resulting from the intense star formation episodes in central regions of ETGs (Arrigoni et al. 2010). Constraining the [Na/Fe] abundance is also key to using the NaI features at 0.81 nm and at 1.14 nm in order to constrain the IMF low-mass end slope (Smith et al. 2015; Zieleniewski et al. 2015; La Barbera et al. 2017).

This paper is organized as follows. In Section 2 we briefly describe the MUSE science verification observations and the reduction of the MUSE data. In Section 3 we introduce the annular and Voronoi-binned aperture spectra that we use in our analysis and describe how we measured in them the strength of standard and IMF-sensitive absorption-line features, which includes also measuring in these spectra the stellar kinematic broadening and the contamination from nebular emission. Based on these measurements, in Section 5 we will then present evidence for a radial variation in the slope of the IMF in M87 and our best constraints for a radial change in the [Na/Fe] abundance, discussing in particular how such an IMF gradient compares with the local variation of the stellar velocity dispersion and other similar trends in the literature. Finally, in Section 6 we draw our conclusions.

2 MUSE OBSERVATIONS AND DATA REDUCTION

NGC 4486 (M87) was observed with MUSE, on 2014 June 28, during the Science Verification run for this instrument. In this paper we consider only the central MUSE observations from programme 60.A-9312 (PI Sarzi) with two 1800 s-long exposures, slightly offset and at a right angle from each other to optimize the treatment of cosmic rays and bad pixels. Each of these on-source exposures were then followed by a 900 s-long exposure in the outskirts of M87 and by an even further sky pointing, approximately 15 arcmin away from the centre.

The final reduction of the science verification data was performed using the v1.6 version of the standard MUSE pipeline, which works on pixel tables. This includes creation of the master bias, flat-field, and arc calibration solutions based on the standard calibrations observed the same night. These were used to prepare the science exposures for post-processing and trace of the spectra on the CCD, where we used the geometric and astrometric solutions from MUSE commissioning runs to transform the location of the spectra into the focal plane spatial coordinates. On the night of the observations of our data, a standard star (CD-32 9927) was observed, which did not return a well suited response function. Therefore, we used a better-

Downloaded from https://academic.oup.com/mnras/article/478/3/4084/4992755 by Biblioteca di Scienze, Università degli studi di Firenze user on 22 April 2021

suited white dwarf (EG 274) from the previous night to create a response function, and applied it to both target exposures.

Sky emission was removed on each exposure separately, using the offset sky field observations. The procedure consists in two steps, where we first created a representative sky spectrum consisting of an estimate of the sky continuum and sky lines. These were then adapted to and removed from each of the science exposures, incorporating the information of the instrumental line spread function for each of the MUSE channels (IFUs). We noticed that better results were achieved if weak OH absorption bands close to wavelength of the laboratory H β line were excluded from the creation of the sky spectrum, and therefore we used a list of skylines starting from 5197.9 Å. Sky-subtracted pixels tables were then merged into a combined table and finally used to create a standard data cube. This encompasses approximately 1 arcmin square sampled in 0.2 arcsec × 0.2 arcsec spaxels and covers the optical domain from about 4749 to 9348 Å with a spectral resolution of $\sim$60 km s^{-1} at 5500 Å (see e.g. Krajnović et al. 2015)

One other major difference from the standard pipeline reduction was in the treatment of the telluric absorptions. When running the final processing of the MUSE pixel tables (task `muse_scipost`, we did not pass a telluric correction function, as we did not have a good template to prepare it. Instead, all spectra analysed in this work were further corrected for atmospheric telluric absorption using the software MOLECFIT (Smette et al. 2015; Kausch et al. 2015). For a given observed spectrum, MOLECFIT computes a theoretical absorption model by fitting regions of the spectrum affected by prominent telluric lines, based on a radiative transfer code, and an atmospheric molecular line data base. The correction was performed by running molecfit on each of the annular-aperture and Voronoi-binned spectra described in Sections 3.1 and 3.2, obtaining subpercent-level fitting residuals in all spectral regions relevant to our study and in particular around those IMF-sensitive features that are most affected by telluric absorption. To illustrate the accuracy of the MOLECFIT correction, in Fig. 1 we show our annular aperture spectra before and after applying this procedure in the spectral region around both the TiO2 and NaI IMF-sensitive features, at 6230 Å and 8190 Å, respectively.

We note that even without considering spatial binning the quality of the MUSE data is already quite good. At the edge of the MUSE field of view (i.e. at a radius of 30 arcsec and for a *V*-band surface brightness of 19.7 mag), 1 h of observing time allowed us to reach a median value for the signal-to-noise ratio (S/N, based on formal uncertainties on the spectra) per spaxel and per wavelength resolution element of 15 and 25 at 5100 Å and 6400 Å, respectively.

3 SPECTRAL ANALYSIS

Detecting a variation in the number of low-mass stars in external galaxies requires spectra of excellent quality. The signature of dwarf stars can indeed be discerned only once high-precision measurements for the strength of several absorption-line features can be secured and analysed together. In the following we therefore combined up to several hundreds or thousands of MUSE spectra in order to probe with high-quality spectra the radial variation of IMF-sensitive features.

3.1 Annular aperture spectra

In order to trace radial gradients for the IMF in M87, we started by exploring whether the spherical symmetry of this galaxy could be exploited and co-added the MUSE spectra in nuclear regions and in eight nearly-circular annular apertures. This was done without applying any redshift correction since M87 displays very little stellar rotation (up to $\sim$20 km s^{-1}) compared to large values for the stellar velocity dispersion (larger than $\sim$250 km s^{-1} within the MUSE field of view; Emsellem, Krajnović & Sarzi 2014, hereafter EKS14). Fig. 2 shows the layout of these apertures on the MUSE reconstructed image of M87, where regions affected by the non-thermal emission from the jet have been excluded. Non-thermal emission from the central active nucleus affects also the central aperture spectrum, which will thus serve only for illustrative purposes. We then proceeded to match these spectra with the PPXF and GANDALF programs (Cappellari & Emsellem 2004; Sarzi et al. 2006) in order to measure the kinematic broadening of the stellar absorption features and check for the presence of ionized-gas emission, both of which are elements to consider when measuring the strength of stellar absorption lines. In order to achieve the best possible match of the stellar continuum, we used the entire MILES

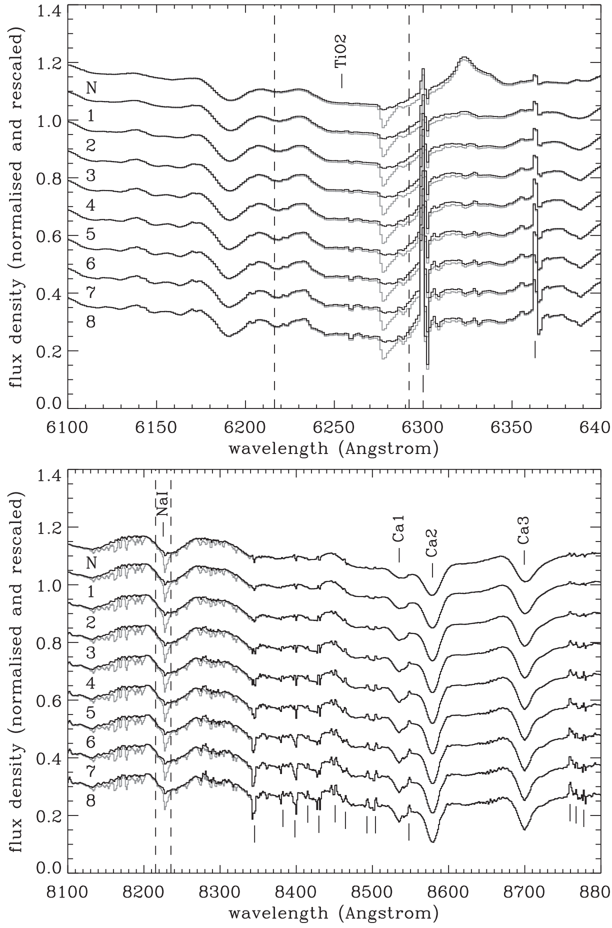

Figure 1. Quality of our correction for telluric atmospheric absorption, as shown by applying the MOLECFIT procedure to the MUSE aperture spectra extracted from the annular regions shown in Fig. 2. These spectra have been normalized and offset for convenience of display, and arranged from top to bottom as a function of distance from the centre of M87. Uncorrected spectra are shown by the grey lines. The top panel shows the wavelength region near the observed position of the TiO2 absorption feature, whereas the lower panel cover the region occupied by both the NaI absorption and Ca triplet. The vertical lines bracket the central passbands defining the IMF-sensitive TiO2 and NaI indices (see Table 2). Spectral regions most affected by sky emission are indicated by the vertical lines plotted below the outer aperture spectrum.

Downloaded from https://academic.oup.com/mnras/article/478/3/4084/4992755 by Biblioteca di Scienze, Università degli studi di Firenze user on 22 April 2021

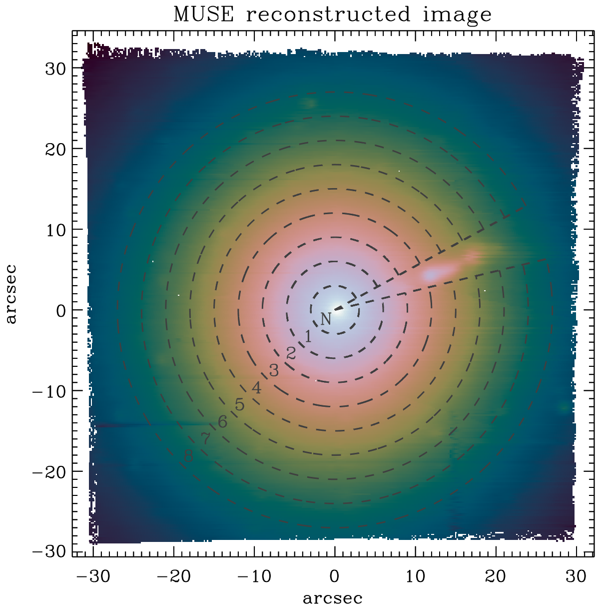

Figure 2. MUSE reconstructed image for the central regions of M87, showing the eight, nearly circular annular regions over which we extracted the aperture spectra shown in Figs 1 and 3. Regions contaminated by synchrotron emission associated with the jet of M87 have been excluded in these apertures. A nuclear spectrum has also been extracted but will only serve for illustrative purposes since such a spectrum is heavily contaminated by non-thermal continuum emission.

Table 1. Aperture spectra basic properties.

ID (1)	Radius (2)	$N_{\rm spax}$ (3)	S/N (4)	S/rN (5)	$\sigma_\star$ (6)
N	<3	675	1465	174	386.2
1	3–6	2033	2294	195	331.3
2	6–9	3379	2625	201	305.9
3	9–12	4739	2774	212	289.4
4	12–15	6094	2793	218	278.9
5	15–18	7470	2768	229	271.4
6	18–21	8792	2703	229	267.1
7	21–24	10 164	2649	229	265.4
8	24–27	11 500	2543	235	265.2

Notes: (1) Aperture number. (2) Radial range, in arcseconds. (3) Number of original 0.2 arcsec × 0.2 arcsec MUSE spaxels within the aperture. (4) Formal S/N ratio (at 5100 Å), as expected from propagation of the statistical uncertainties returned by the data reduction. (5) Observed S/rN value reached by our best GANDALF fits (over the entire fitted range). (6) Stellar velocity dispersion, in km s^{-1}, as returned by our PPXF fit.

stellar library (Sánchez-Blázquez et al. 2006; Falcón-Barroso et al. 2011) during both the PPXF and GANDALF fits, while also adopting a 10th-order polynomial correction, additive and multiplicative for PPFX and GANDALF, respectively. Consistently with EKS14, the PPXF fit was restricted to the 5050–6000 Å wavelength range, whereas the present GANDALF fits extended from 4800 to 6850 Å.

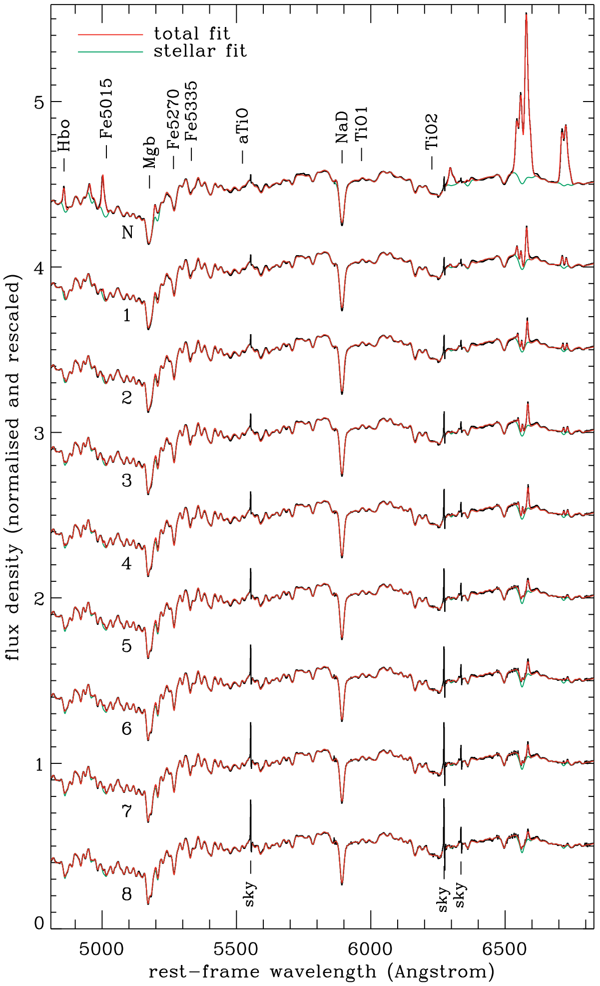

Figure 3. MUSE aperture spectra extracted from the annular regions shown in Fig. 2 over the wavelength range of our GANDALF fit (red and green lines for total and stellar fit only, respectively). These spectra have been normalized and offset for convenience of display, and arranged from top to bottom as a function of distance from the centre. The position of the adopted IMF-sensitive absorption features (see Table 2) that fall in this wavelength range is also shown, together with that of the NaD doublet that responds to the [Na/Fe] abundance and of the classical Hb, Mgb, Fe5270, and Fe5335 Lick indices that will serve to constrain the stellar age, metallicity, and the abundance of α-elements. Regions affected by sky emission (at an observed wavelength of 5577, 6300, and 6330 Å) have been omitted in the fit.

The basic properties of these nine aperture spectra are listed in Table 1, whereas Fig. 3 shows our best GANDALF fit to them. Our models appear to match quite well such spectra, which are all of very good quality as expected considering that our apertures encompass several hundreds to thousands single MUSE spectra. Based on the propagation of the statistical uncertainties on the flux density values of the MUSE spectra, we should indeed be able to reach very high formal values for the S/N ratio, between 1500 and 2500, in our annular aperture spectra. Yet, the level of fluctuations in the residuals of our best GANDALF fit greatly exceeds such purely statistical errors, with residual-noise levels that lead to signal-to-residual-noise values (S/rN) around just 240. The quality of PPXF is considerably higher, thanks to the use of additive polynomials and of a smaller fitting range, but again this leads to S/rN ∼ 340 that are still quite short of the formal S/N expectations. Such a discrepancy cannot simply be ascribed to intrinsic limitations in the modelling of the stellar continuum. For instance, in the case of Sloan Digital Sky Survey (SDSS) data, Johansson et al. (2014) could reach much higher S/rN values (around ∼500) when using the MILES library to fit high S/N stacked spectra of galaxies. Instead, the discrepancy between formal S/N and observed S/rN values relates most likely to small instrumental differences between the 24 integral-field units in MUSE or to correlations between adjacent spaxels introduced by

Downloaded from https://academic.oup.com/mnras/article/478/3/4084/4992755 by Biblioteca di Scienze, Università degli studi di Firenze user on 22 April 2021

interpolation processes in the MUSE data reduction (see also, e.g. García-Benito et al. 2015, for the case of CALIFA data).

3.2 Voronoi-binned spectra

Given the previous shortcomings in co-adding the MUSE spectra over such large spatial regions as our annular aperture we decided to measure the strength of absorption-line features also in Voronoi-binned spectra similar to those that served to map the stellar kinematics of M87 in EKS14. For this we used the algorithm of (Cappellari & Copin 2003) to spatially bin our MUSE spectra to a target S/N = 300 as done in EKS14 and then proceeded to fit those spectra with PPXF and GANDALF as we did for our annular templates except as stellar templates were concerned. In fitting the Voronoi-binned spectra we indeed use the optimal templates that result from the best combinations of the MILES stellar templates obtained during our PPXF and GANDALF fits to the annular aperture spectra, using such optimal templates for the corresponding PPXF and GANDALF fits to our binned spectra. The quality of these fits is also quite high, with average S/rN values of around 230 and 130 for the PPXF and GANDALF fits, respectively. These S/rN do not differ much from those measured in our annular apertures, which again is indicative of systematic variations across the MUSE field that do not average out when spectra are combined in very large apertures, in addition to spatial correlations introduced during the data reduction and inherent limitations in our stellar continuum modelling.

Since the S/rN values obtained in the annular-aperture spectra do not significantly exceed the corresponding S/rN values in the Voronoi-binned spectra we do not expect the former spectra to lead to particularly tighter constraints on the slope of the IMF. On the other hand, the finer spatial sampling of the Voronoi-binned spectra allows us to better investigate radial IMF trends. Furthermore, given the circular symmetry of M87, the Voronoi-binned spectra effectively provide independent radial index measurements that could be used to derive realistic estimates for the error in our line-strength measurements and thus, eventually, for low-mass end slope of the IMF at any given radius.

For these reasons we will use the Voronoi-binned spectra to carry out our stellar-population analysis (Section 4), and use the annular-aperture spectra only for illustrative purposes in the remainder of this section.

3.3 Line-strength measurements

For all extracted spectra, we measured the strength of several IMF-sensitive features such as aTiO, TiO1, and TiO2 in the optical, as well as the strength of calcium triplet (using the Ca1, Ca2, and Ca3 indices) and of the NaI$\lambda\lambda$8183, 8195 absorption lines in the near-Infrared. Moreover, we measured line-strengths for the classic Mgb, Fe5015, Fe5270, Fe5335 Lick indices in order to constrain the metallicity and [Mg/Fe] abundance ratio, as well as the strength of NaD$\lambda\lambda$5890, 5896 doublet, which is key to gauging [Na/Fe] abundance ratios. We also measured H$\beta_{\rm o}$, a modified Hβ index designed to minimize the age–metallicity degeneracy (Cervantes & Vazdekis 2009). The Mgb, Fe5270, Fe5335 indices were combined into the total metallicity indicator $[{\rm MgFe}]' = [{\rm Mgb} \times (0.72 \times {\rm Fe5270} + 0.28 \times {\rm Fe5335})]^{1/2}$ defined in Thomas, Maraston & Bender (2003), which we used in our analysis together with the combined iron index $\langle {\rm Fe} \rangle = (Fe5270 + Fe5335)/2$. For aTiO, we followed the index definition of Spiniello et al. (2014), but took care to interpolate the spectra in the rest-frame wavelength region between λ = 5542.4 and 5559.6 Å in order to exclude the residuals from the subtraction of the bright [O I] 5577 sky emission line. Notice that when comparing observations to predictions of stellar-population models (Section 4.2), the same interpolation is also applied to the models before measuring line-strength indices. For TiO1, we followed the Lick definition, while for both TiO2 and NaI, we used the definitions of La Barbera et al. (2013) where in particular for TiO2 the red pseudo-continuum passband was slightly modified to avoid sky-subtraction residuals from the prominent [O I] 6300 sky line.

Table 2. Definition of the most IMF-sensitive indices adopted in this study.

Index (1)	λ_{bb}–λ_{br} (2)	λ_{cb}–λ_{cr} (3)	λ_{rb}–λ_{rr} (4)	Ref. (5)
aTiO	5420.0–5442.0	5445.0–5600.0	5630.0–5655.0	1
TiO1	5816.6–5849.1	5936.6–5994.1	6038.6–6103.6	2
TiO2	6066.6–6141.6	6189.6–6265.0	6422.0–6455.0	3
NaI	8143.0–8153.0	8180.0–8200.0	8233.0–8244.0	3
Ca1	8474.0–8484.0	8484.0–8513.0	8563.0–8577.0	4
Ca2	8474.0–8484.0	8522.0–8562.0	8563.0–8577.0	4
Ca2	8619.0–8642.0	8642.0–8682.0	8700.0–8725.0	4

Notes: (1) Index name. (2) Blue and red wavelength limit for the blue pseudo-continuum passband. (3) Blue and red wavelength limit for the index passband. (4) Blue and red wavelength limit for the red pseudo-continuum passband. (5) Source for the index definition: 1 – Spiniello et al. (2014), 2 – Trager et al. (1998), 3 – La Barbera et al. (2015), 4 – Cenarro et al. (2001).

The definition of our main IMF-sensitive absorption features is summarized in Table 2, with their position indicated in Figs 1 and 3. Notice that in this work we analyse all three calcium-triplet lines separately, rather than combining them up into a single line strength. Since the three Ca lines respond differently to the [Ca/Fe] abundance and the IMF slope this approach allows us to disentangle the two effects, circumventing the need for bluer Ca spectral features such as Ca4227 that do not fall within the MUSE spectral range (see Mentz et al. 2016, for details).

All index measurements were carried out without performing any smoothing of the observed spectra. Instead, during the stellar-population analysis, for each spectrum we convolved the stellar-population models by the stellar velocity dispersion measured during the PPXF fit, which in the case of Voronoi bins yields a stellar kinematics that is entirely consistent with the one published in EKS14. This approach extracts the maximum amount of information from the data, and avoids possible contamination of the relevant absorption-line features from the residuals of the subtraction of nearby sky lines when instead all observed spectra are smoothed to the same stellar velocity dispersion. We also did not place our indices on the Lick system, as we rely on stellar-population models based on flux calibrated stellar spectra (i.e. the MILES stellar library).

Finally, we flagged and excluded from the remainder of our analysis all Voronoi-binned spectra showing the presence of emission lines affecting our absorption line-strength indices or with a significant contribution from the non-thermal continuum associated with either the jet or the active nucleus of M87. As regards nebular emission, despite the well-known presence of ionized-gas emission in M87 (e.g. Macchetto et al. 1996; Sarzi et al. 2006) we note that none of our chosen IMF-sensitive indices (Table 2) could be affected by it. On the other hand accounting for the presence of nebular emission lines is crucial for our age, metallicity, and [α/Fe] abundance estimates, in particular due to Hβ, [O III]$\lambda\lambda$4959, 5007 and [N I]$\lambda\lambda$5197, 5200 emission entering the H$\beta_{\rm o}$, Fe5015 and Mgb

Downloaded from https://academic.oup.com/mnras/article/478/3/4084/4992755 by Biblioteca di Scienze, Università degli studi di Firenze user on 22 April 2021

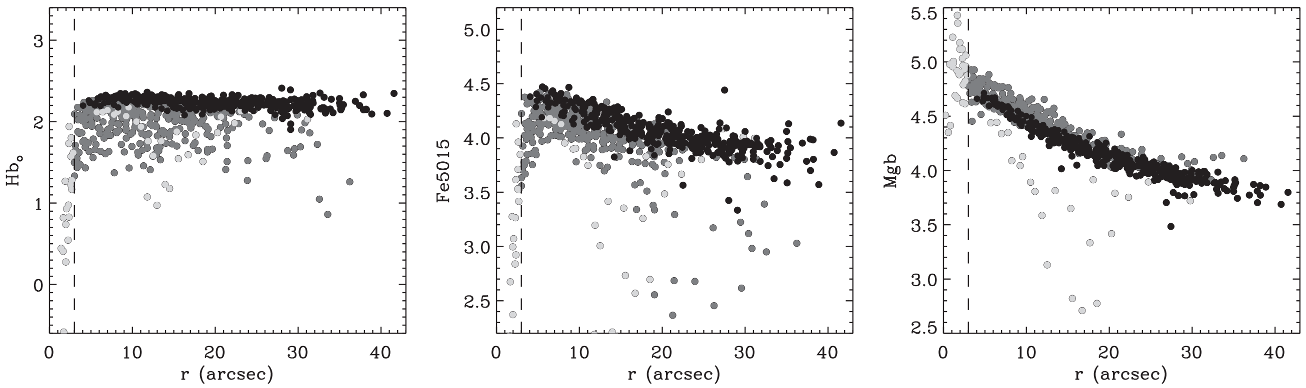

Figure 4. Radial profiles for the strength of the H β_o, Fe5015, and Mgb Lick absorption-line indices that enter our stellar age, metallicity, and α-elements abundance measurements, as measured in our Voronoi-binned spectra (Section 3.2). The dark grey points in each panel show Voronoi bins that will be excluded from our analysis due to the adverse impact of nebular emission, whereas the light grey points indicate bins discarded due to the presence of a non-thermal continuum associated either to the jet or AGN of M87. Such a featureless continuum tends to dilute absorption lines and decrease the value of their corresponding line-strength indices, similar to the case of line infill from H β and [O III] in the case of the H β_o and Fe5015 indices, respectively. [N I] emission, on the other hand, falls on the red continnum passband of the Mgb index and thus leads to an artificial increase of its value. The index values shown here were computed after bringing the Voronoi-binned spectra to a common kinematic broadening corresponding to a stellar velocity dispersion of 360 km s^{-1}, in order to allow a direct comparison at different galactic radii.

indices, respectively. Based on our GANDALF fit results we decided to take a rather conservative approach and flagged Voronoi-binned potentially affected by H β, [O III] and [N I] emission only when the much stronger [N II]$\lambda\lambda$6548, 6584 lines were comfortably detected. Such a conservative approach proved more reliable compared to the standard procedure for judging the detection based on the value for the line amplitude to residual-noise level ratio *A*/*rN* (Sarzi et al. 2006), and is further justified considering the old age of the stellar population of M87 and thus for the need to deal with even very small amounts of emission-line infill, in particular for the H β_o index. As for the non-thermal continuum, we excluded bins inside a radius of 3 arcsec and along the jet direction, that is, within 7° of its direction at a PA = −69° (as shown in Fig. 2). The adverse impact of both nebular emission and the jet/AGN non-thermal continuum on our H β_o, Fe5015 and Mgb indices can be appreciated in Fig. 4, which otherwise display rather tight and smooth radial gradients.

3.4 Line-strength gradients

Focusing on all but two of our key IMF-sensitive features and on the NaD index (which is also somehow sensitive to the IMF), Fig. 5 allows already to appreciate the radial variation for their strength across our annular aperture spectra. This is then shown more quantitatively by Fig. 6 where the line-strength values are plotted against radius for the Voronoi-binned spectra, excluding at this point regions affected by nebular emission or a jet/AGN non-thermal continuum as discussed in Section 3.3. Fig. 6 shows that all our IMF-sensitive absorption-line indices display clear radial gradients, which also allows to identify Voronoi-bins to be further excluded from our analysis (mostly at the edge of the MUSE field of view), whenever the values for the line-strength indices are found to be significant (at a 3σ level) outliers from a third-order polynomial fit to the observed radial trend. Fig. 6 also shows that the index values determined in the annular aperture spectra agree fairly well with the median values computed from the Voronoi bins at the same radial intervals, well within the scatter of these last measurements that will also serve as errors for our stellar-population analysis.

The radial gradients shown in Figs 5 and 6 may already indicate a variation in both the IMF slope and the [Na/Fe] abundance, although gradients in stellar metallicity or the abundance of α-elements ([α/Fe]) could also contribute to them. For instance, Spiniello et al. (2014) shows that the strength of the aTiO, TiO1, and TiO2 indices increases not only with the IMF slope but also with [α/Fe]. Similarly, the NaD index responds very strongly to metallicity in addition to the abundance of sodium, whereas classical metallicity- or [α/Fe]-sensitive indices such as Fe5270 and Mgb are far less sensitive to the IMF slope. In fact, no single IMF-sensitive index allow to directly estimate the IMF slope, and in order to constrain the low-mass end of the IMF this parameter has to be optimized together with at least the stellar metallicity and [α/Fe] abundance (for an old galaxy such as M87) while matching the strength of several spectral features that together carry enough information on all these stellar-population properties, as detailed below.

4 STELLAR-POPULATION ANALYSIS

4.1 Stellar-population models

To constrain the stellar-population content of M87 we compared the observed strength of the absorption-line indices in our MUSE spectra to predictions from the MIUSCAT stellar-population models (Ricciardelli et al. 2012; Vazdekis et al. 2012). More specifically, for each Voronoi-binned spectrum of M87, we compared observed and model absorption-line strengths derived after smoothing the MIUSCAT models to the observed values for the stellar velocity dispersion of the given spectrum, as obtained from PPXF (see Section 3.3).

The MIUSCAT models cover the spectral range between 3465 and 9469 Å at a nominal resolution of 2.51 Å (FWHM Falcón-Barroso et al. 2011) and provide state-of-art simple stellar-population (SSPs) predictions based on the empirical stellar libraries, namely the MILES library in the optical range ($\lambda\lambda$3525−7500 ; Sánchez-Blázquez et al. 2006) and the CaT library in the near-infrared ($\lambda\lambda$8350−9020; Cenarro et al. 2001). The Indo-US library (Valdes et al. 2004) is then used to fill the gap between MILES and CaT. The models rely on solar-scaled isochrones (either Padova00 or BaSTi; from Girardi et al. 2000 and

Downloaded from https://academic.oup.com/mnras/article/478/3/4084/4992755 by Biblioteca di Scienze, Università degli studi di Firenze user on 22 April 2021

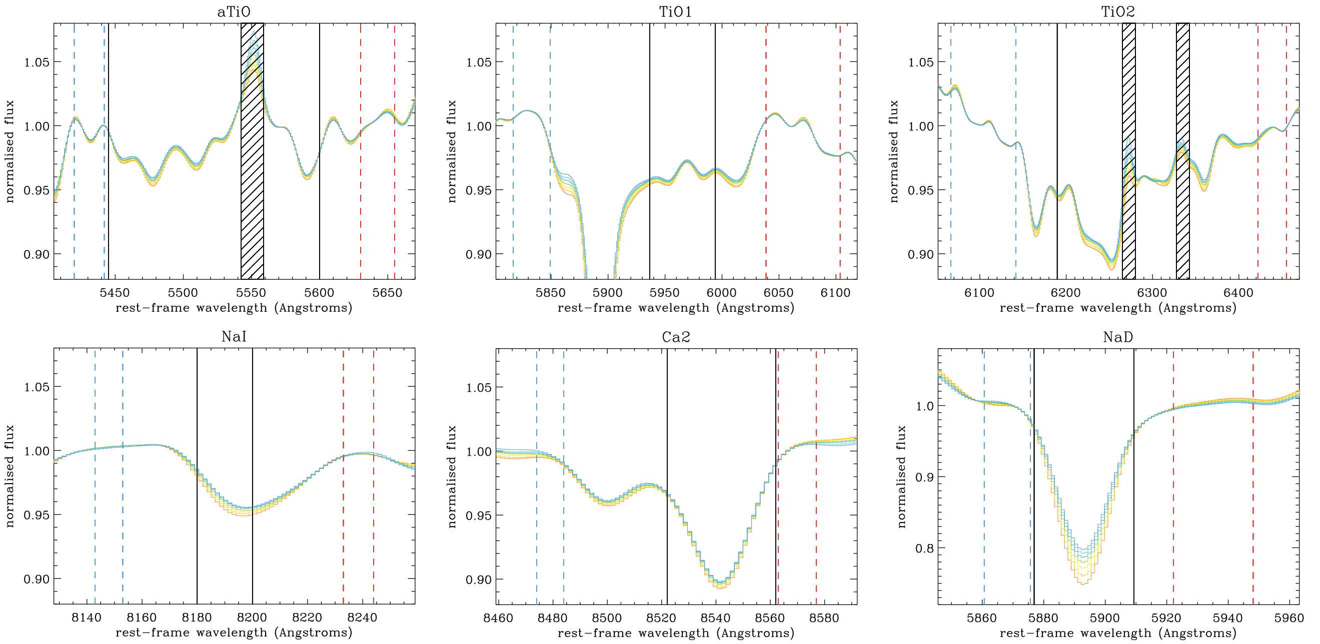

Figure 5. Detailed view of the annular aperture spectra of Fig. 3 (excluding the nuclear spectrum) illustrating the radial variation for the strength for the IMF-sensitive absorption-line features aTiO, TiO1, TiO2, NaI, and Ca2, as well as for the NaD absorption on which our [Na/Fe] estimates will be based. In each panel, the aperture spectra are colour-coded according to the radial distance they probe and have been brought to a common kinematic broadening corresponding to a stellar velocity dispersion of 360 $\mathrm{km\,s^{-1}}$. Vertical solid lines indicate the index bandpass, whereas the blue and red dashed lines the blue and red continuum regions, respectively (see Table 2). All spectra are normalized to the pseudo-continuum level in the index bandpass. Vertical hatched boxes show regions affected by sky emission. The Ca1 and Ca3 features show similarly clear variations to Ca2 and are omitted here for clarity.

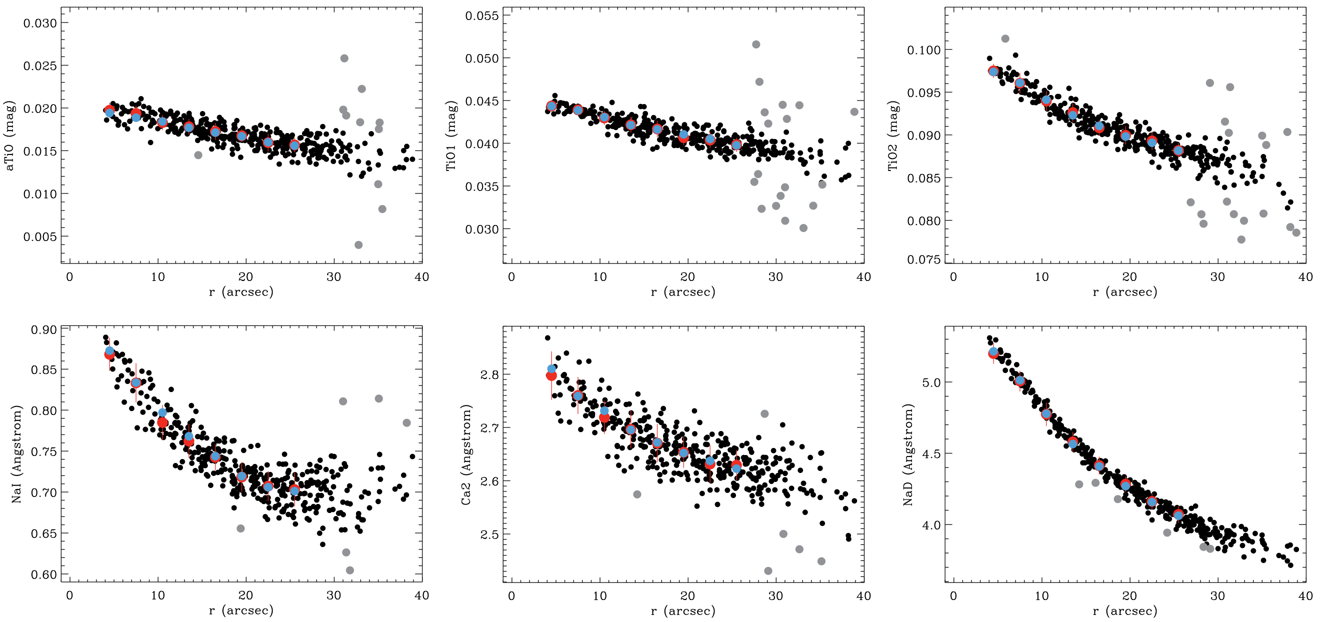

Figure 6. Radial trend for the values of the IMF-sensitive aTiO, TiO1, TiO2, NaI, and Ca2 indices and for the NaD index, as measured in our annular aperture spectra (blue bullets) or in Voronoi-binned spectra with formal S/N of 300 (black & grey small bullets). The red bullets with errors bars show the median values of the latter measurements and their scatter, which provides a conservative estimate of the uncertainties in our index measurements given the circular symmetry of M87. The index values shown here were computed after bringing the spectra to a common kinematic broadening corresponding to a stellar velocity dispersion of 360 $\mathrm{km\,s^{-1}}$, in order to allow a direct comparison for strength of absorption lines at different galactic radii (for our analysis indices are measured on the original spectra, see Section 3.3). Voronoi bins significantly affected by the non-thermal continuum associated with the jet and AGN of M87, or by nebular emission, are not shown and were not used to compute the mean and standard deviations on the Voronoi-bin measurements. The grey points show 3σ outliers from a third-order polynomial fit to the radial gradients of all line-strength indices used in this work, which are also excluded during our analysis.

Downloaded from https://academic.oup.com/mnras/article/478/3/4084/4992755 by Biblioteca di Scienze, Università degli studi di Firenze user on 22 April 2021

Pietrinferni et al. 2004, respectively), and are based on stellar spectra following the abundance pattern of our Galaxy, i.e. approximately solar-scaled at Solar metallicity and α-enhanced at metallicities below Solar (Bensby, Feltzing & Oey 2014). For comparison with our previous works (e.g. La Barbera et al. 2013; Spiniello et al. 2014), we base our analysis on MIUSCAT models with Padova isochrones. The MIUSCAT SSPs cover a wide range of ages, from 0.06 to 17.78 Gyr, and seven metallicity bins, i.e. [Z/H]$= -2.32$, -1.71, -1.31, -0.71, -0.4, 0.0, and +0.22. SSPs models are provided also for several IMFs either unimodal (single power-law) or 'bimodal' (low-mass tapered) in flavour, which are both characterized by their slope, Γ (unimodal) and Γ_{b} (bimodal), as a single free parameter (see e.g. Vazdekis et al. 1996, 2003). The 'bimodal' IMFs are smoothly tapered off below a characteristic 'turnover' mass of $0.6\,\mathrm{M}_{\odot}$. For $\Gamma_{\mathrm{b}} \sim 1.3$, the low-mass tapered IMF gives a good representation of the Kroupa IMF, while for $\Gamma \sim 1.3$ the unimodal IMF coincides with the Salpeter distribution. The lower and upper mass-cutoff of the IMFs are set to 0.1 and $100\,\mathrm{M}_{\odot}$, respectively (see also fig. 3 of La Barbera et al. 2013, for an illustration of these two IMF parametrizations). Notice that low-mass tapered IMFs have been shown to provide a better description of the optical and NIR spectral features in ETGs (La Barbera et al. 2016), and of their mass-to-light ratios (Lyubenova et al. 2016). Therefore, we base the present analysis on MIUSCAT SSPs with a low-mass tapered distribution.

4.2 Fitting line-strengths

As a first step, we proceeded to estimate the stellar age, metallicity, and the [α/Fe] abundance ratio by applying the same approach as in La Barbera et al. (2013, hereafter LB13). We start by estimating the stellar age and metallicity in each of our Voronoi bins from the $\mathrm{H}\,\beta_{\mathrm{o}}$–[MgFe]$'$ diagram, minimizing the rms of observed and model line-strengths over a grid of SSP model predictions, interpolated over a fine grid with steps of 0.05 Gyr in age and 0.006 dex in metallicity. Then, at fixed age, we compute the solar-scaled proxy for [α/Fe], measured as the difference between metallicity estimates from the Mgb and $\langle$Fe$\rangle$ line-strength indices. Such a proxy is calibrated on to [α/Fe] with the aid of Thomas, Maraston & Johansson (2011a) stellar-population models, as detailed in LB13, resulting into an excellent accuracy (rms) of about 0.025 dex in [α/Fe]. Notice that while the [α/Fe] could be also estimated relying on α-enhanced stellar-population models (e.g. Vazdekis et al. 2015), such models do (partly) rely on theoretical atmosphere predictions, while the proxy approach is entirely based on the empirical (MIUSCAT) models. Moreover, the LB13 method for deriving [α/Fe] is independent of the adopted IMF (see La Barbera et al. 2016, for more details). Fig. 7 shows the $\mathrm{H}\,\beta_{\mathrm{o}}$–[MgFe]$'$ diagram for the Voronoi-binned MUSE spectra on which our analysis is based, which excludes bins affected by nebular emission, a non-thermal continuum associated with either the jet or AGN of M87 (see Fig. 4), or where systematic effects (mostly near the edge of the MUSE field) led to unreliable line-strength measurements (see Fig. 6). Notwithstanding the well-known difficulties in matching the strength of the $\mathrm{H}\,\beta$ absorption line, relating for instance on the impact of individual elements abundance on the $\mathrm{H}\,\beta$ line (such as [C/Fe]; Conroy & van Dokkum 2012a) or the well-known uncertainty in tracing the response of Balmer lines to theoretical spectra featuring different line lists (see e.g. section 5.3 of Vazdekis et al. 2015), the $\mathrm{H}\,\beta_{\mathrm{o}}$–[MgFe]$'$ diagram of Fig. 7 shows that all spectra of M87 are consistent with a very old age and a radial trend that indicates the characteristic negative metallicity gradient observed in ETGs. This is also consistent with a preliminary analysis of our MUSE spectra with the STARLIGHT spectral fitting code of Cid Fernandes et al. (2005). In the following we will therefore considered only MIUSCAT models with an old age of 14 Gyr, although we verified that none of the main conclusions of this work change if we adopt a different age value or consider age as an extra fitting parameter while constraining the IMF slope (see also, e.g. the case of La Barbera et al. 2016). In particular, we note that if the data in Fig. 7 suggest the presence in M87 of a positive age gradient and slightly younger central stellar populations (which unfortunately would be difficult to assess given how the data fall systematically below the solar-scaled grid at all radii), should this be the case we would infer an even steeper IMF gradient than by assuming a constant old age, thus reinforcing the conclusions of our analysis.

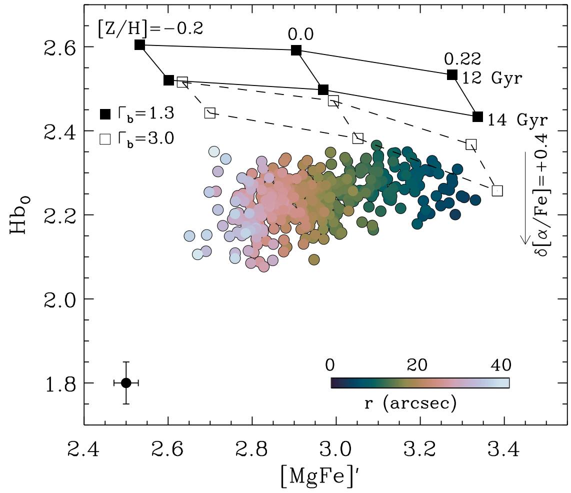

Figure 7. $\mathrm{H}\,\beta_{\mathrm{o}}$–[MgFe]$'$ index–index diagram as measured in our final sample of Voronoi-binned spectra, that is, by excluding regions affected by nebular emission, a non-thermal continuum associated the AGN and/or jet of M87 (see Fig. 4) or where systematic effects led to unreliable line-strength measurements (see Fig. 6). Shown are also MIUSCAT model grids for varying stellar age and metallicity, drawn with solid and dashed lines for a Kroupa IMF (corresponding to a $\Gamma_{\mathrm{b}} = 1.3$, see Section 4.1) and for a bottom-heavy IMF ($\Gamma_{\mathrm{b}} = 3.0$), respectively. The impact of an enhanced α-element is also shown by the downward-pointing vertical arrow (from the models of Vazdekis et al. 2015). The data points are colour-coded according to distance from the centre, which highlights the presence of a well-established negative metallicity gradient in ETGs. Typical errors are also shown at the lower left corner of this figure.

Having constrained the stellar age, metallicity and – most important – the [Mg/Fe] ratio in our Voronoi-binned spectra, we proceed to estimate the slope of the low-mass tapered IMF, Γ_{b}, following a similar procedure to LB13 and La Barbera, Ferreras & Vazdekis (2015). Specifically, we minimize the expression:

$$\chi^2([\mathrm{Z/H}], \Gamma_{\mathrm{b}}, [\mathrm{X/Fe}]) = \sum_i \left[\frac{E_{\mathrm{corr},i} - E_{\mathrm{M},i} - \sum_{\mathrm{X}} \Delta_{i,\mathrm{X}} \cdot [\mathrm{X/Fe}]}{\sigma_i} \right]^2, \qquad (1)$$

where $E_{\mathrm{corr},i}$ are the observed absorption-line strengths for a selected set of spectral features (e.g. IMF-sensitive features) corrected to Solar-scale based on our [Mg/Fe] estimates, $E_{\mathrm{M},\,i}$ are model absorption-line strengths for the same features, [X/Fe] is the abundance ratio of different chemical elements and $\Delta_{i,\mathrm{X}}$ is the sensitivity of the ith absorption-line index to a given elemental abundance, i.e. $\Delta_{i,\mathrm{X}} = \delta(E_{\mathrm{M},\,i})/\delta([\mathrm{X/Fe}])$. Finally σ_i is the uncertainty on $E_{\mathrm{corr},i}$, ob-

Downloaded from https://academic.oup.com/mnras/article/478/3/4084/4992755 by Biblioteca di Scienze, Università degli studi di Firenze user on 22 April 2021

tained by adding in quadrature the error on our E_i (as derived from the azimuthal variation at different radii, see Section 3.4) with the uncertainty on our correction to a Solar scale.

As regards the latter, we bring the observed absorption-line strengths E_i to a Solar scale following LB13, that is, we derived the trend of a given index with [Mg/Fe] from SDSS stacked spectra of ETGs at fixed stellar velocity dispersion and use our previous estimate of [Mg/Fe] in our Voronoi-binned spectra to correct the value of the considered index to its [Mg/Fe] = 0 value. For this reason, the abundance ratios obtained from equation(1) should be interpreted as residual abundances rather than absolute estimates of [X/Fe]. The advantage of this approach, as opposed to relying entirely on models with varying [X/Fe] (such as, e.g. those of Conroy & van Dokkum 2012a), is that one relies as much as possible on empirical trends rather than on more uncertain theoretical model calculations. As for the $E_{\mathrm{M},i}$, these are computed with MIUSCAT models of varying metallicity and IMF slope, while the $\Delta_{i,\mathrm{X}}$ values are derived from the publicly available stellar-population models of Conroy & van Dokkum, taking models with a Solar metallicity, old age (t = 13.5 Gyr) and a Kroupa IMF. Notice also that since the Conroy & van Dokkum models are computed at fixed Fe abundance rather than total metallicity [Z/H], when applying the $\Delta_{i,\mathrm{X}}$ terms in equation (1) one is actually changing the metallicity content of MIUSCAT models, which enters the $E_{\mathrm{M},i}$ values. Therefore, when solving for the IMF slope through equation (1) we need to allow the total metallicity be an extra fitting parameter, rather than fixing it to the best-fitting value from the H β_{o}–[MgFe]′ diagram. Similarly, since the abundance of single elements is optimized while we look for the best IMF slope, the best-fitting values of [Z/H] from equation (1) should not be interpreted as 'true' estimates of [Z/H]. To summarize, although the free fitting parameters in equation (1) are total metallicity [Z/H], IMF slope Γ_{b} and elemental abundances [X/Fe], in practice our procedure is designed only to provide an estimate for the IMF slope.

In order to prove the robustness of our results, we have performed the χ^2 determination procedure using different combinations of IMF-sensitive indices and including different sets of element abundance [X/Fe]. As shown below, we find that our main result, i.e. the presence of a radial IMF gradient in M87, is independent of the method adopted. Finally, as regards the uncertainties on our best-fitting parameters, these were obtained by a bootstrapping approach, whereby the fitting is repeated after shifting the observed-line strengths and the values of [MgFe] (used to correct indices to [MgFe] = 0, see above) according to their uncertainties.

5 RESULTS

5.1 IMF, metallicity, and [α/Fe] abundance gradients

We start discussing the results of our stellar-population modelling by showing in Fig. 8 the radial profiles for the best-fitting slope Γ_{b} for a low-mass tapered 'bimodal' IMF, as obtained by minimizing the expression given by equation (1) while using different sets of absorption-line indices and while either holding or varying the abundance elements.

As a first step, in panel (a) of Fig. 8 we show that a tight Γ_{b} gradient is found even when simply using only the optical IMF-sensitive indices TiO1, TiO2, and aTiO and while holding the abundance of all elements at a Solar scale. Γ_{b} is also found to be steeper at all radii than $\Gamma_{\mathrm{b}} = 1.3$, which corresponds to the case of a Kroupa, Milky Way-like IMF. Since a varying [Ti/Fe] abundance may contribute to the observed TiO1, TiO2, and aTiO gradients (Fig. 5) that in turn lead us to infer a varying IMF slope, in panel (b) we then show what happens when we let the [Ti/Fe] ratio free. During this step we also include the Fe5015 index in our analysis since this index responds negatively to the [Ti/Fe] abundance (Thomas et al. 2011a; La Barbera et al. 2015), so that adding Fe5015 helps in breaking the degeneracy between IMF slope and [Ti/Fe] abundance. Additionally, in panel (c) we exclude the aTiO index since this is a rather broad absorption-line feature thus making the value of the aTiO index particularly sensitive to the accuracy of our relative flux calibration. Either ways, panels (b) and (c) show very similar Γ_{b} profiles to the one corresponding to our simplest approach of panel (a), which gives us confidence both in our treatment of the [Ti/Fe] abundance and in our aTiO measurements.

Next, in panel (d) of Fig. 8 we vary the [O/Fe] abundance in addition to the [Ti/Fe] abundance, while using the TiO1, TiO2, and Fe5015 indices but still leaving out aTiO as in panel (c). In panel (e) we then further include the IMF-sensitive Ca1, Ca2, and Ca3 indices while allowing also for a varying [Ca/Fe] abundance, while in panel (f) we add the popular but IMF-sensitive NaI index, for which we also need to account for [Na/Fe] variations that in turn are better constrained when including also the NaD index in equation (1). While panel (d) still shows an IMF gradient, the Γ_{b} values now decrease more gently with radius and are significantly lower (on average by 0.4) compared to what observed in panel (c) when only the [Ti/Fe] abundance was varied, which is expected given that both TiO1 and TiO2 respond positively to the [O/Fe] abundance. The Γ_{b} profiles of panels (e) and (f) are then remarkably similar to those of panel (d), which shows that both Ca and Na features point to a radial IMF gradient consistent with that inferred from TiO features. This consistency also confirms the quality of our correction for telluric absorption (Fig. 1).

Finally, in panels (g), (h) and (i) we show how by reintroducing the aTiO index in our analysis brings back the Γ_{b} values to levels similar to those observed in the top panels of Fig. 8 where the [O/Fe] abundance was not varied, which reflects the fact that aTiO responds weakly or negatively to [O/Fe] and thus the importance of including it to disentangle the effects of [O/Fe] and IMF. Although not shown here for the sake of clarity, we also checked the robustness of our results on the TiO1 and TiO2 features, by excluding these two indices altogether from the fitting procedure and while removing also Fe5015 and fixing [Ti/Fe] and [O/Fe] to Solar values. Also in this case we found a clear IMF gradient very much in line with the previously discussed cases.

Overall, the upshot from Fig. 8 is that irrespective of our choice for the set of IMF-sensitive indices to include in our analysis and for the set of elements abundance that we decided to vary, one always finds that in the central region of M87 probed by our MUSE observations the slope Γ_{b} for a low-mass tapered 'bimodal' IMF steeply decreases with radius, corresponding to a fraction of low-mass stars that remains above what found in the Milky Way.

Even though the model presented in panel (i) of Fig. 8 could be regarded as our best and final model, given that it includes the largest set of IMF-sensitive indices and of varying element abundances, we prefer to combine the IMF results from our different model approaches and thus present in Fig. 9 (left-hand panel) a more conservative view of the IMF gradient in M87, which is also meant to capture systematic effects both in our data and in stellar-population models. The scatter around such combined Γ_{b} values is still relatively small, however, with average 68 per cent confidence limits of 0.28. This also does not largely exceed average formal Γ_{b} errors on our single model approaches, which range between ∼0.1

Downloaded from https://academic.oup.com/mnras/article/478/3/4084/4992755 by Biblioteca di Scienze, Università degli studi di Firenze user on 22 April 2021

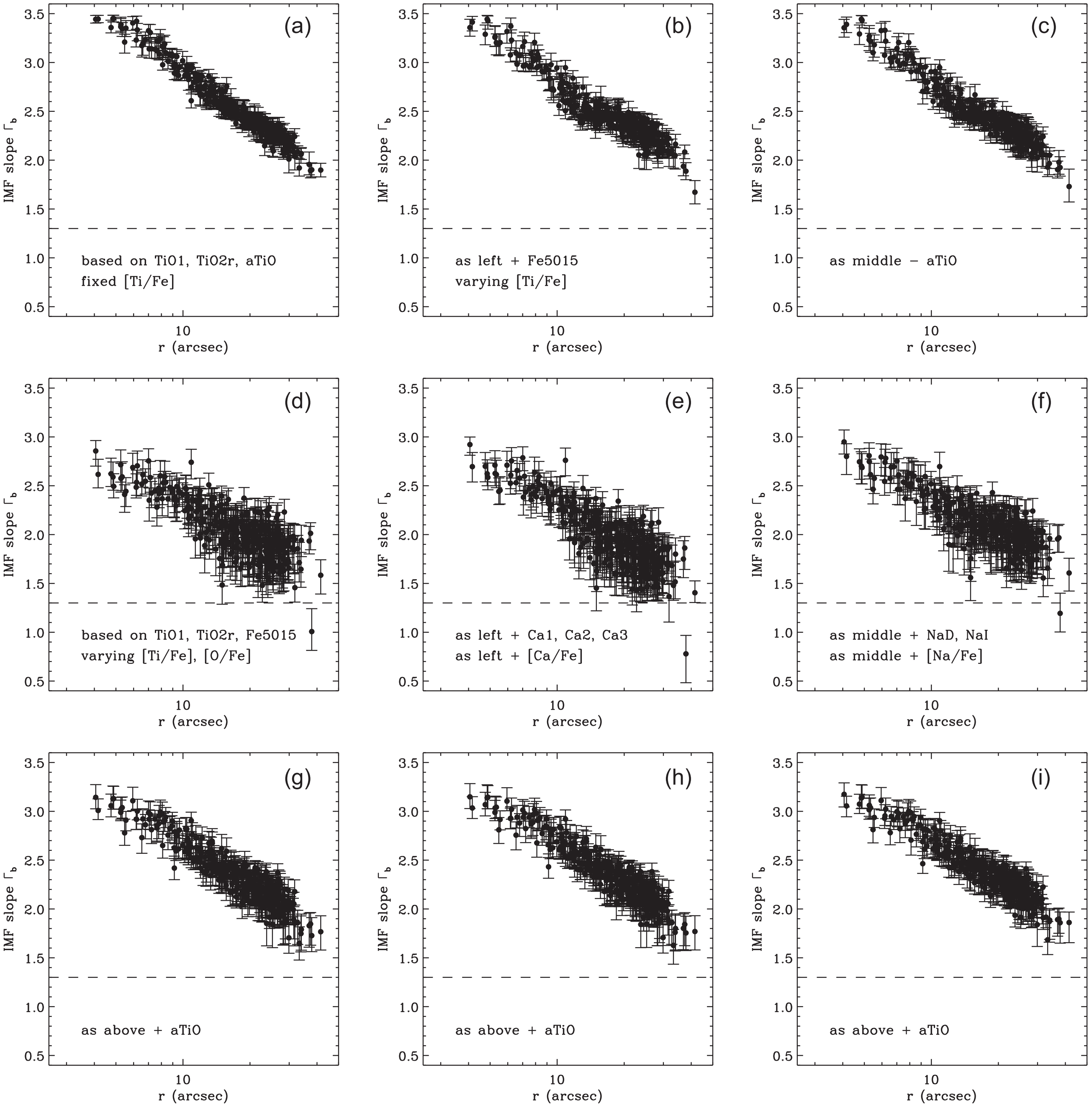

Figure 8. Radial profiles for the best-fitting slope Γ_b for a low-mass tapered 'bimodal' IMF, obtained by minimizing the expression given by equation (1) while using different sets of absorption-line indices and by either holding or varying the abundance of different elements. Irrespective of the latter choices the IMF slope Γ_b is always found to decrease with radius and to display values well above $\Gamma_b = 1.3$ as in the case of a Milky Way like, Kroupa IMF (horizontal lines).

and ∼0.2 and could be regarded as the limiting accuracy on IMF measurements that may be achieved with MUSE.

Fig. 9 (middle and right-hand panels) also shows our best values for the stellar metallicity [Z/H] and α-element abundance [α/Fe], which both exhibit rather tight and negative gradients with a scatter of just ∼0.02 dex. The observed metallicity gradient is in line with the typical decrease of −0.28 dex per decade in radius observed in ETGs (e.g. Kuntschner et al. 2010) and both our central, luminosity-weighted [Z/H] and [α/Fe] values (see Fig. 9) agree well the SAURON measurements of McDermid et al. (2015) inside one-eighth of the effective radius ($R_e/8 = 10.2$ arcsec, taking R_e= 81.2 arcsec as in Cappellari et al. 2011). At larger radii, however, our [Z/H] gradient is somehow steeper than the one found by McDermid et al., who also report little or no evidence for a gradient in [α/Fe] in M87 (consistent with the previous SAURON analysis in this object by Kuntschner et al. 2010). As regard the discrepancy in [α/Fe] between us and McDermid et al., we have verified that accounting for such differences (e.g. by artificially increasing [α/Fe] in our model by 0.1 dex) would lead only to negligible changes the Γ_b values (e.g. by a few per cent) inferred at large radii. Consid-

Downloaded from https://academic.oup.com/mnras/article/478/3/4084/4992755 by Biblioteca di Scienze, Università degli studi di Firenze user on 22 April 2021

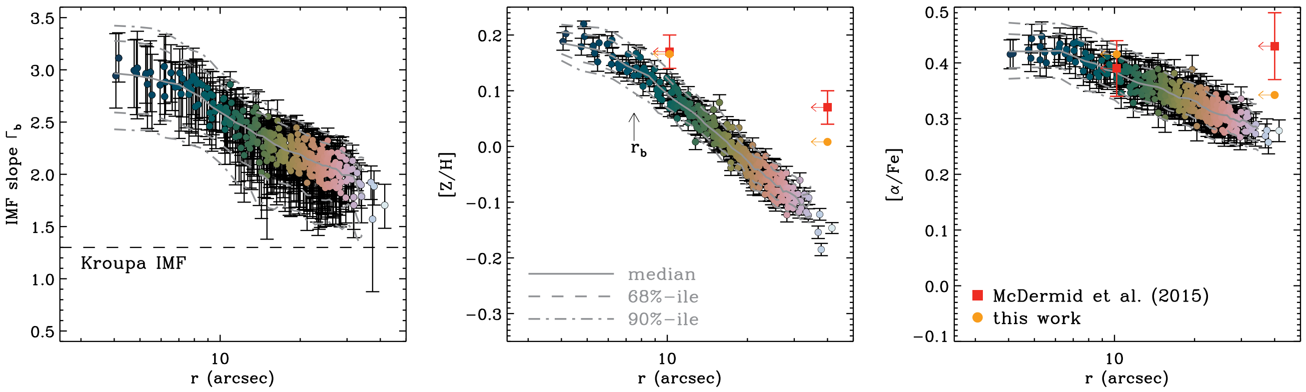

Figure 9. Final radial profiles for the best-fitting slope Γ_b for a low-mass tapered 'bimodal' IMF (left-hand panel), as obtained from combining the results based on different combinations of absorption-line indices and while either holding or varying the abundance of various elements (see Fig. 8), as well as for the stellar metallicity [Z/H] and the α-elements abundance [α/Fe] (middle and right-hand panels, respectively). In each panel the grey solid line shows median values within 3 arcsec-wide radial bins, whereas the grey dashed and dot–dashed lines show the 68 per cent and 90 per cent confidence levels around such a median, respectively. Points are colour-coded according to distance from the centre of M87 as in Fig. 7 and the horizontal dashed line in the left-hand panel shows the Γ_b value for a Kroupa IMF, as in Fig. 8. In the middle and right-hand panels, the two orange circles and red squares, each with a leftward-pointing arrow, indicate the luminosity-weighted [Z/H] and [α/Fe] values inside $R_e/8$ and $R_e/2$, as computed here (after extrapolating the gradients up to r= 2 arcsec) and in McDermid et al. (2015, based on SAURON data), respectively. The vertical arrow in the middle panel indicate the break radius r_b where the surface brightness flattens and departs from a single Sérsic profile (see fig. 4 of Côté et al. 2006).

ering studies that have investigated IMF radial variation we note that our [α/Fe] profile would also appear at odds with the rather flat [α/Fe] trend reported by van Dokkum et al. (2017) for their sample galaxies. Their objects probe a wide range of stellar metallicities, however, and one needs to keep in mind that in this regime the [α/Fe] estimates depends on the underlying abundance pattern of the stellar library used to produce stellar-population models, which might, by itself, introduce differences among [α/Fe] estimates based on different models (i.e. MIUSCAT versus Conroy & van Dokkum models).

Interestingly, the metallicity gradient appears to change slope and flatten at around the same distance of 7.5 arcsec where the surface brightness profile of M87 departs from a single Sérsic law and we observe the onset of a central core, as generally found in the most massive ETGs (Ferrarese et al. 2006, but see also Fig. A1). Such a coincidence would be consistent with the idea that galactic cores result from the scouring of the central stellar regions due to the formation of a supermassive black hole binary during a merger event (e.g. Milosavljević & Merritt 2001), as indeed one would expect to also find a similar flattening of any pre-existing gradient for the stellar-population properties. In fact, we note that both the IMF and [α/Fe] gradient seems also to flatten towards the centre, although [Z/H] appears still to follow more closely the surface brightness than Γ_b or [α/Fe]. The values of the Spearman's rank coefficient ρ for a correlation between the surface brightness and [Z/H], Γ_b and [α/Fe] are indeed 0.97, 0.87, and 0.89, respectively, and are all highly significant.

Given such similarities between the radial trends shown in Fig. 9, it is perhaps not surprising to find in Fig. 10 (top panel) that our MUSE measurements for M87 parallel rather well the IMF–metallicity relation that Martín-Navarro et al. (2015c) derived using both resolved (from Martín-Navarro et al. 2015a and from the CALIFA survey, Sánchez et al. 2012) and unresolved measurements (from SDSS data) in ETGs. Even though the agreement with the IMF–metallicity trend of Martín-Navarro et al. supports their suggestion that the IMF shape is more tightly connected to the stellar metallicity then to other stellar-population parameters or physical quantities such as stellar velocity dispersion, we first of all note that in our case the Γ_b also follows [α/Fe] fairly well (Fig. 10, middle panel). Furthermore, if there are reasons to consider the role of metallicity in determining the local stellar mass spectrum (e.g. given that conversely metal-poor systems show evidence for a top-heavy IMF, Marks et al. 2012) we note that in first place the metallicity gradient of ETGs was likely set up by the local depth of the potential well during the same very intense and short episode of star formation that led to enhanced [α/Fe] ratios throughout the galaxy (see e.g. Pipino et al. 2010). This is indeed particularly evident when the stellar metallicity is compared with the luminosity-weighted predictions for the escape velocity $V_{\rm esc}$, either globally (Davies et al. 1993) or locally within galaxies (Scott et al. 2009, 2013).[1] On the other hand, our MUSE measurements (Fig. 10, lower panel) confirm the finding of Martín-Navarro et al. that the local stellar velocity dispersion σ does not trace well the radial variation of the IMF in ETGs. In M87 this is particularly evident since the σ radial profile reaches a plateau at around 265 km s^{-1} from a radius of ∼20 arcsec onward (Table 1, but see also Fig. A1 in Appendix A), whereas the Γ_b values continue to decrease beyond this point (just like our [Z/H] and [α/Fe] values do, see also Fig. 9).

5.2 Mass-to-light ratio and mismatch parameter

In order to further compare our results with previous IMF studies, including those based on dynamical constraints for the IMF, we evaluate the mass-to-light ratio M/L that corresponds to our best stellar-population results. Similarly, we also compute the so-called mismatch parameter $\alpha_{\rm IMF}$ by taking the ratio of our best M/L values to those that would correspond to a Milky Way-like IMF while holding to our best stellar age, metallicity and [α/Fe] estimates. Fig. 11 (top panel) shows the radial profile for our best M/L estimates

---

[1] In this respect, we note that our Γ_b values follow the $V_{\rm esc}$ values provided by the models of Scott et al. (2013) just as well as they follow our [Z/H] estimates (with a Spearman's rank coefficient ρ = 0.87), even though a proper comparison between IMF slope and $V_{\rm esc}$ would require the latter to be computed self-consistently on the basis of mass models accounting for a varying mass-to-light ratio.

Downloaded from https://academic.oup.com/mnras/article/478/3/4084/4992755 by Biblioteca di Scienze, Università degli studi di Firenze user on 22 April 2021

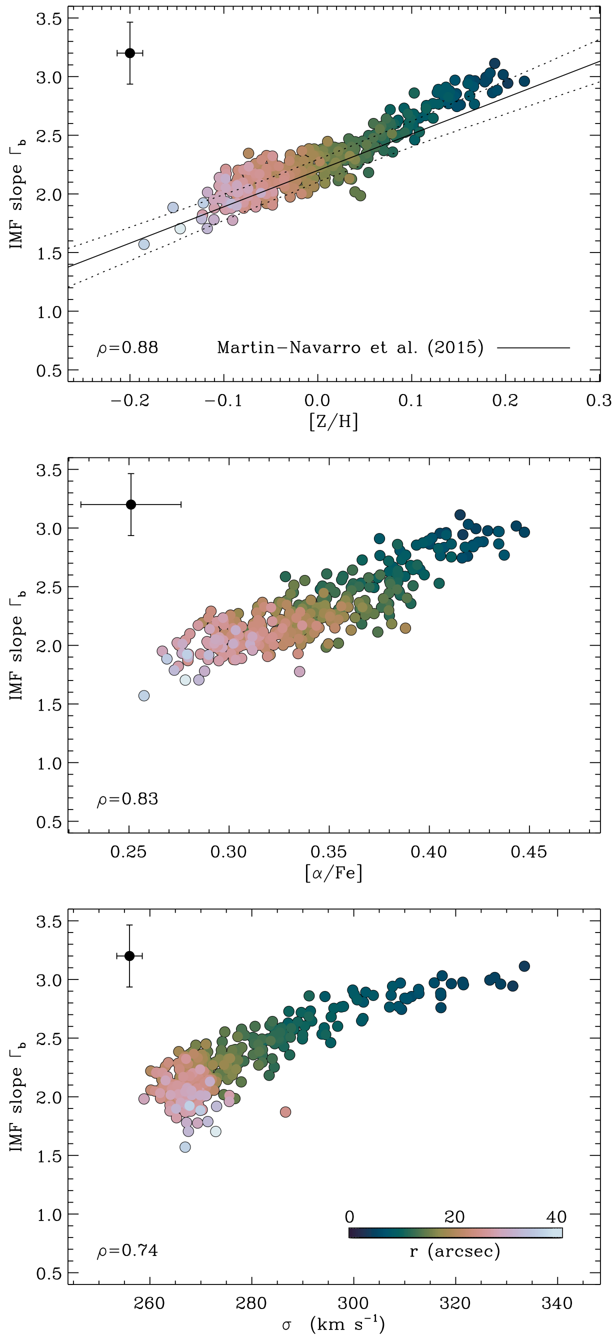

Figure 10. Correlations between the inferred slope Γ_b for a low-mass tapered 'bimodal' IMF and our measurements for the stellar metallicity [Z/H] (top panel), α-elements abundance [α/Fe] (middle panel) and stellar velocity dispersion σ (lower panel). In each panel the typical errors in both plotted quantities are shown in the top left corner, whereas the value of the Spearman's rank correlation coefficient ρ is reported in the lower left corner. Data points are colour-coded according to distance from the centre as in Fig. 7. The top panel also shows IMF–metallicity relation of Martín-Navarro et al. (2015c), which our MUSE data seem to follow rather well. Even though such an agreement supports the idea that the IMF shape is more tightly connected to the stellar metallicity then to other stellar-population parameters, in the case of M87 the Γ_b values would appear to follow fairly well also the [α/Fe] values (middle panel). On the other hand, our analysis confirms that σ is not a particularly good tracer for the radial variation of the IMF in ETGs.

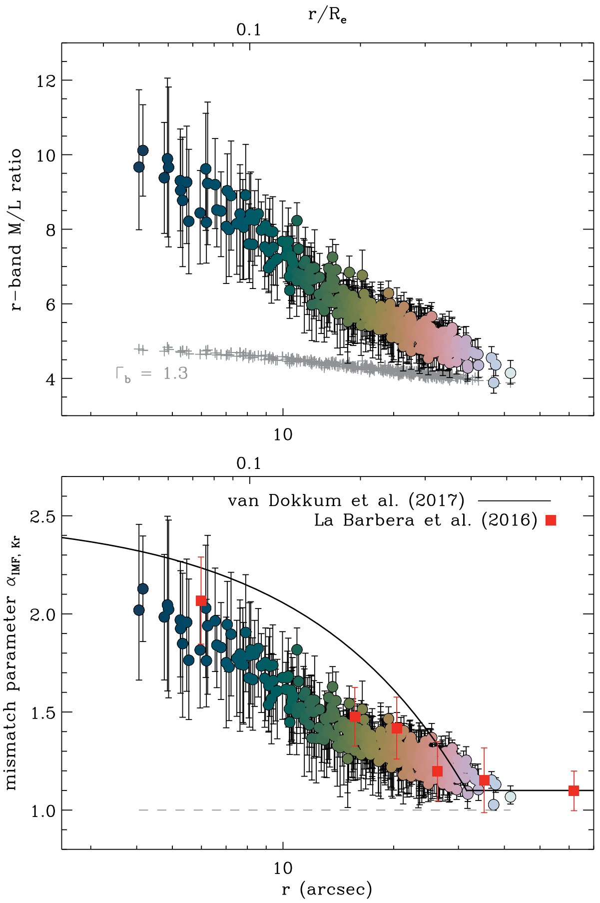

Figure 11. Radial profile for the r-band stellar mass-to-light ratio (top panel) and mismatch parameter α_{IMF} (lower panel) corresponding to our best-fitting slope Γ_b of a low-mass tapered 'bimodal' IMF, as well as to our best values for the stellar metallicity and [α/Fe] ratio. The grey points in top panel show the $(M/L)_{\mathrm{Kr}}$ values corresponding to a Kroupa IMF (when $\Gamma_b = 1.3$), which also serves to compute the mismatch parameter $\alpha_{\mathrm{IMF,\,Kr}} = (M/L)/(M/L)_{\mathrm{Kr}}$ that is shown in the lower panel where the grey horizontal line indicates the case of a Kroupa IMF. In the lower panel our $\alpha_{\mathrm{IMF,\,Kr}}$ profile is also compared to the mean trend recently inferred by van Dokkum et al. (2017) and to the $\alpha_{\mathrm{IMF,\,Kr}}$ gradient measured by La Barbera et al. (2016) in the early-type galaxy XSG1. To this effect at the top of each panel we also show the radial scale in units of the effective radius R_e.

in the SDSS r-band as well as the r-band $(M/L)_{\mathrm{Kr}}$ values that would correspond to a Kroupa IMF, which allows to evaluate the mismatch parameter $\alpha_{\mathrm{IMF,\,Kr}} = (M/L)/(M/L)_{\mathrm{Kr}}$ as a function of radius (lower panel).

The presence of a higher fraction of low-mass stars towards the centre of M87 has a strong impact on the projected M/L values, more than doubling M/L from 40 to 4 arcsec and well exceeding what would derive from changes only in stellar metallicity or α-element abundance. Such a dramatic M/L variation ought to be included in dynamical models, in particular when considering that intrinsically, i.e. when deprojected, the M/L gradient in M87 is likely to be even steeper and to extend to even higher M/L values towards the centre. For instance, giving more weight to stars in the central regions of M87 may help with the current tension between gas- and stellar-dynamical measurements for the mass of the central supermassive black hole, where the latter have historically exceeded the former by nearly a factor two (see e.g. Oldham & Auger 2016 and Gebhardt et al. 2011 versus Walsh et al. 2013 and Macchetto et al. 1997).

Downloaded from https://academic.oup.com/mnras/article/478/3/4084/4992755 by Biblioteca di Scienze, Università degli studi di Firenze user on 22 April 2021

In the lower panel of Fig. 11 we also compare our $\alpha_{\rm IMF,\,Kr}$ radial profile to the mean trend found by van Dokkum et al. (2017) for their sample of six ETGs and to the $\alpha_{\rm IMF,\,Kr}$ gradient measured by La Barbera et al. (2016) in the galaxy XSG1, both of which were derived through a stellar-population analysis. The $\alpha_{\rm IMF,\,Kr}$ profile matches fairly well the gradient observed in XSG1, which is also a very massive ETG like M87, and remarkably agree with both the average trend reported by van Dokkum et al. and the data of La Barbera et al. in that by approximately 0.4–0.5 R_e also in M87 we observe a nearly Milky Way-like IMF. As we approach the centre our $\alpha_{\rm IMF,\,Kr}$ values systematically fall below the line drawn by van Dokkum et al., however. This discrepancy may relate to their different parametrization for the IMF whereby the low-mass end of the IMF is allowed to vary (in two stellar-mass m regimes between 0.08 $M_\odot < m < 0.5$ $M_\odot$ and 0.5 $M_\odot < m < 1.0$ $M_\odot$), thus effectively resembling more like a unimodal form and hence possibly leading to larger M/L values. Yet, we also note that there are significant differences between the $\alpha_{\rm IMF,\,Kr}$ gradients observed in each of the van Dokkum et al. targets. For instance, one of the two most massive objects in their sample, NGC 1600, shows a flatter $\alpha_{\rm IMF,\,Kroupa}$ gradient reaching up to central values similar to what we find in M87.

Turning now our attention to dynamical measurements of the IMF slope based on direct estimates for the stellar M/L ratio, in Fig. 12 we compare our radial profile for the mismatch parameter with both the global estimates from the ATLAS$^{\rm 3D}$ survey (Cappellari et al. 2013) and the recent resolved measurements in M87 by Oldham & Auger (2018). More specifically, in the top panel of Fig. 12 we plot the r-band mismatch parameter rescaled with respect to a Salpeter IMF $\alpha_{\rm IMF,\,Sa}$ against stellar velocity dispersion σ, in order compare our findings with both the corresponding $\alpha_{\rm IMF,\,Sa}$ and σ global values (within 1R_e) for M87 and to the trend between these same quantities acrossed different ETGs (red square in Fig. 12). Overall our $\alpha_{\rm IMF,\,Sa}$ value are consistent with the global ATLAS$^{\rm 3D}$ data point, as the luminosity-weighted integrated measurements inside $R_e/8$ and $R_e/2$ (orange points) appear on course to fall not too far off from the ATLAS$^{\rm 3D}$ measurement within R_e. However, as in the case of the IMF slope (Fig. 10, lower panel), the stellar velocity dispersion traces the mismatch parameter only in the central regions. Furthermore, $\alpha_{\rm IMF,\,Sa}$ increase with σ faster than it is observed from integrated measurements across different galaxies, further suggesting that σ is not an optimal tracer for IMF variations in ETGs.

In the lower panel of Fig. 12 we show the radial profile of our V-band mismatch parameter with respect to a Chabrier IMF $\alpha_{\rm IMF,\,Ch}$ in order to compare this profile to the corresponding gradient from the dynamical and stellar-population models for M87 of Oldham & Auger, which is presently a unique study in that it allows for a radially varying M/L ratio in their dynamical models. Although the $\alpha_{\rm IMF,\,Ch}$ values of Oldham & Auger lie systematically below ours (on average by a factor 1.3), their $\alpha_{\rm IMF,\,Ch}$ gradient parallels very well our $\alpha_{\rm IMF,\,Ch}$ profile. Such an offset most likely originates from the requirement of the Oldham & Auger models that the dynamical M/L values reach those expected for a Chabrier IMF towards the outer parts of M87, which for them corresponds to regions 20 arcsec ($\sim$ 1.5 kpc) away from the centre where our stellar-population analysis still indicates an excess of low-mass stars compared to the case of the Milky Way. On the other hand, we also note that such a level of discrepancy falls within the systematic factors involved in this kind of comparison between spectral and dynamical constraints of the IMF. Indeed, for several of their objects Lyubenova et al. (2016) report spectral mismatch parameter estimates that exceed the values of their dynamical counterparts, by up to ∼25 per cent. Despite the offset, the remarkable agreement in the slope of the two independently-derived radial profiles for the mismatch parameter shown in Fig. 12 gives us more confidence on our model assumption for a low-mass tapered ‘bimodal’ IMF in M87. High-quality data such as those presented here may indeed reveal systematic IMF variations across different objects that could depend on factors yet to be identified.

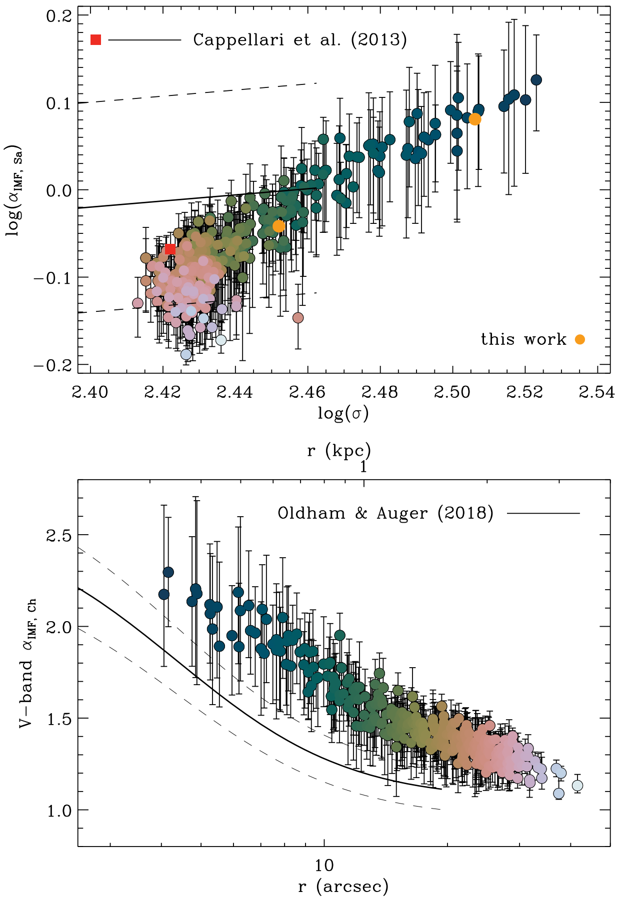

Figure 12. Top panel: r-band mismatch parameter rescaled with respect to a Salpeter IMF and plotted against stellar velocity dispersion σ in order to be compared to the global value for $\alpha_{\rm IMF,\,Sa}$ in M87 (red square) and across different ETGs, (solid and dashed lines) as function of global stellar velocity dispersion (within 1 R_e) as derived through dynamical and stellar-population modelling over the course of the ATLAS$^{\rm 3D}$ survey (Cappellari et al. 2013). As in Fig. 9 the orange circles correspond to our luminosity-weighted integrated measurement inside $R_e/8$ and $R_e/2$. Lower panel: radial profile for the V-band mismatch parameter with respect to a Chabrier IMF $\alpha_{\rm IMF,\,Ch}$ compared to the predictions for this same quantity by Oldham & Auger (2018), who allow for a varying M/L ratio in their dynamical models. Although systematically below our values, the $\alpha_{\rm IMF,\,Ch}$ gradient of Oldham & Auger parallels remarkably well our $\alpha_{\rm IMF,\,Ch}$ profile.

5.3 The [Na/Fe] abundance

The behaviour of optical to near-infrared sodium spectral features in massive galaxies has recently received significant attention, not only in relation to their sensitivity to the low-mass end of the IMF (in particular for the NaI 0.81 and 1.14 nm features, see e.g. Conroy & van Dokkum 2012a; Spiniello et al. 2014; Smith et al. 2015; Zieleniewski et al. 2015; McConnell et al. 2016; La Barbera et al. 2017)

Downloaded from https://academic.oup.com/mnras/article/478/3/4084/4992755 by Biblioteca di Scienze, Università degli studi di Firenze user on 22 April 2021

but also in connection to the detection of interstellar absorption and the possible presence of cold-gas outflows (around the Na D lines at 0.59 nm, see e.g. Jeong et al. 2013; Park, Jeong & Yi 2015; Sarzi et al. 2016; Nedelchev, Sarzi & Kaviraj 2017). Yet, tackling the importance of a possible variation in [Na/Fe] abundance is critical to properly interpreting the observed strength of sodium features and thus draw conclusions on the IMF slope or on the properties of the ISM. Super-solar [Na/Fe] abundance patterns are indeed to be expected in massive ETGs as a result of their short star formation histories since similar to the case of α elements, sodium is mainly produced in Type II supernovae (Tsujimoto et al. 1995). Furthermore, the presence of a bottom-heavy IMF in the low-mass tapered ‘bimodal’ form that we considered, may make the contribution of intermediate-mass stars (between 3 and 8 $\mathrm{M}_{\odot}$) in their asymptotic giant branch (AGB) phase quite relevant (Ventura et al. 2013; La Barbera et al. 2017).

In the MUSE spectral range the classical Na D Lick index is the most sensitive to changes in the [Na/Fe] abundance, responding also strongly to stellar metallicity and only mildly to the [α/Fe] abundance and the shape of low-mass end of the IMF. This makes the NaD index ideal to trace the [Na/Fe] abundance as a function of radius in M87, which is also known to contain little or no dust (e.g. Baes et al. 2010).

To constrain [Na/Fe] abundance ratios, we rely on the Na-MILES stellar-population models recently implemented by La Barbera et al. (2017, hereafter LB17), which provide SSPs with varying [Na/Fe], up to ∼1.2 dex and over the same range of age, total metallicity, and IMF slope as in the extended MILES models of Vazdekis et al. (2015) For each of our Voronoi-binned spectra in M87, we first correct the Na D line strength to a Solar [α/Fe] = 0 scale, using the following equation:

$$\mathrm{Na\,D_{corr}} = \mathrm{Na\,D} \cdot (1 + \alpha_{\mathrm{Na\,D}} \cdot [\alpha/\mathrm{Fe}])^{-1}, \quad (2)$$

where

$$\alpha_{\mathrm{Na\,D}} = \frac{\delta(\mathrm{Na\,D})/\mathrm{Na\,D}}{\delta[\alpha/\mathrm{Fe}]} = -0.83 \quad (3)$$

is the relative response of the Na D index to [α/Fe]. The value of $\alpha_{\mathrm{Na\,D}}$ was empirically determined in LB17 and the fact that α_{NaD} is negative shows that the NaD index decreases with [α/Fe] (see e.g. Conroy & van Dokkum 2012a). Then, we derive the value of [Na/Fe] of the Na-MILES SSP model prediction that fits better the $\mathrm{NaD_{corr}}$ values, by fixing age, metallicity, and IMF slope Γ_b to the best-fitting values that were previously derived in the given spectrum. In order to estimate the uncertainty on [Na/Fe], we reiterate such a [Na/Fe] mimization procedure by shifting the values of metallicity, IMF slope, and [α/Fe] according to their uncertainties.

Fig. 13 shows the results of this procedure, which returns [Na/Fe] abundance values well above Solar in the central regions of M87 probed by our MUSE observations (that is, within $R_e/2$) and a considerable negative [Na/Fe] gradient of around 0.15 dex per decade in radius. Such high [Na/Fe] values can be explained considering that Na is primarily made in massive stars and ejected in Type II supernovae, whereas Type Ia explosions produce very little of it (Tsujimoto et al. 1995). Furthermore, intermediate-mass AGB stars ($3 < M/\mathrm{M}_{\odot} < 8$) may have also returned significant amounts Na in a short period of time (less than a 1 Gyr). Thus, similar to the case of α-elements, the observed super-Solar [Na/Fe] values relate almost certainly to the short time-scales over which the stars in massive galaxies such as M87 are thought to have formed.

The inferred [Na/Fe] values indeed follow rather well the radial [α/Fe] profile shown in Fig. 9 although we note that the [Na/Fe] gradient is somewhat steeper than the [α/Fe] gradient. To put it in another way, the [Na/α] ratio, which takes SN Ia out of the picture and traces more directly the yields of SN II, increases towards the centre. This behaviour could relate to metallicity, which would boost the secondary production of Na in SN II through neutron-capture processes while having only a limited impact on the SN II yields of α-elements (e.g. Kobayashi et al. 2006). If the metallicity gradient of M87 was also put in place early-on while the bulk of its stars formed (Pipino et al. 2010), then it is possible that the early ISM was further enriched in Na towards the centre thanks to metal-rich SN II. In this respect, intermediate-mass AGB stars may have played a role too, since their Na yields are also predicted to increase with metallicity (Ventura et al. 2013). On the other hand, we note that these results contrast with the finding of La Barbera et al. (2017) in the massive ETG XSG1, where the [Na/Fe] radial profile inside $R_e/2$ is found to be similarly flat to that of the [α/Fe] ratio despite the presence of a significant metallicity gradient. Hopefully the origin of such a discrepancy will become clear as the number of ETGs with resolved gradient abundance of Na and other elements increases.

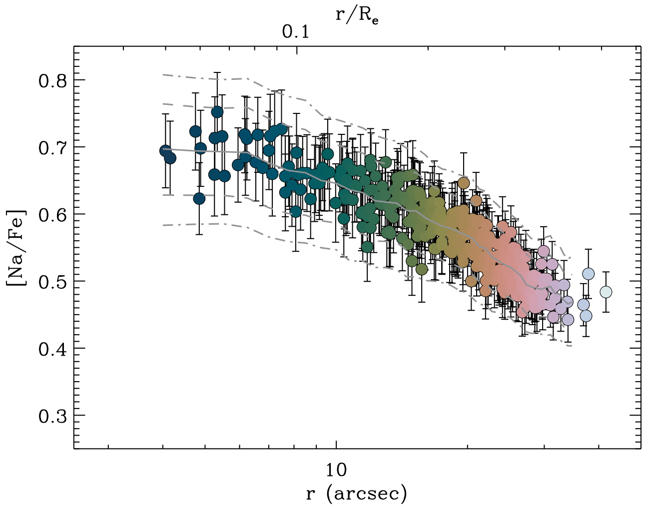

Figure 13. Radial profile for the [Na/Fe] abundance in M87, as derived in our Voronoi-binned spectra. As in Fig. 9 the grey solid line shows median values within 3 arcsec-wide radial bins, whereas the grey dashed and dot–dashed lines show the 68 per cent and 90 per cent confidence levels around such a median. Data points are also colour-coded according to distance from the centre as in Fig. 7.

To conclude this section we note that also the [Na/Fe] profile shows a flattening towards the central regions, as observed for the Γ_b, [Z/H] and [α/Fe] profiles plotted in Fig. 9. This further supports a scenario whereby the stellar-population properties of M87 may have once shown steeper gradients towards the centre, taking the present shape during the formation of a supermassive black hole binary and the scouring of central stellar regions that led to the flattening of the surface brightness profile observed in this massive galaxy.

6 CONCLUSIONS

Using MUSE integral-field spectroscopic data for the central regions of the giant elliptical NGC 4486 we have investigated the low-mass end of the stellar IMF in its stellar population. For this we have followed the approach of La Barbera et al. (2013, 2015) to match the predictions of state-of-the-art stellar-population models to the strength of various absorption-line features that are sensitive to

Downloaded from https://academic.oup.com/mnras/article/478/3/4084/4992755 by Biblioteca di Scienze, Università degli studi di Firenze user on 22 April 2021

the fraction of dwarf stars, as observed after binning our data to a target S/N = 300 and in regions unaffected by non-thermal or nebular emission. Assuming a constant stellar age of 14 Gyr and a ‘bimodal’, low-mass tapered form for the IMF where the slope Γ_b above a mass of 0.6 $M_\odot$ is free to vary, after solving for the best metallicity [Z/H] and α-elements abundance [α/Fe] we find that

(i) M87 displays a significant negative IMF gradient inside $R_e/2$, with $\Gamma_b > 1.3$ at all radii indicative of an excess of low-mass stars compared to the case of the Milky Way, in particular towards the innermost regions.

(ii) The presence of such an IMF gradient is robust against the choice of the IMF-sensitive features that we include in our analysis (between aTiO, TiO1, TiO2, NaI, and the Ca triplet features) and the set of elements abundance (among Ti, O, Na and C) that we decided to vary.

(iii) The IMF slope Γ_b is found to closely follow the [Z/H] values, consistent with the findings of Martín-Navarro et al. (2015c), who suggested that metallicity traces IMF variations better than other stellar-population or physical properties.

(iv) The stellar velocity dispersion σ, on the other hand, does not trace well the Γ_b gradient in M87, further suggesting that locally, σ is not a good tracer of IMF variations in ETGs (see also van Dokkum et al. 2017).

(v) The observed IMF gradient corresponds to a dramatic variation in the value of the projected stellar mass-to-light ratio M/L in M87, which more than doubles between 4 and 40arcsec, our probed radial range.

(vi) Accounting for variations due to changes in [Z/H] or [α/Fe], this M/L gradient corresponds to a radial profile for the mismatch parameter α which indicates that by $R_e/2$ there is only a mild excess of low-mass stars compared to what found in the Milky Way. Put together with the recent works of La Barbera et al. (2016) and La Barbera et al. (2017), our results in M87 further suggests that IMF variations are a very central phenomenon in ETGs.

(vii) Remarkably, our α profile parallels very well the one derived by Oldham & Auger (2018) in M87 based on M/L measurements from dynamical models. This agreement further supports the choice for a bi-modal parametrization for the IMF over a uni-modal form, adding to similar comparisons between dynamical and spectral IMF measurements by La Barbera et al. (2016) and Lyubenova et al. (2016).

In addition to constraining radial variations for the IMF in M87 we also estimated the abundance of sodium, not only because this is key to interpreting the strength of near-IR IMF-sensitive features such as NaI 0.81 nm and NaI 1.14 nm but also since tackling the [Na/Fe] abundance could have bearings on ISM studies based on the Na D interstellar absorption. Following the method of La Barbera et al. (2017) we find that:

(i) M87 displays an Na abundance well above Solar inside $R_e/2$, reaching to [Na/Fe] values around 0.7 dex towards the centre, and a considerable negative [Na/Fe] gradient of 0.15 dex per decade in radius.

(ii) While such [Na/Fe] values are most likely the result of a short star formation history and the prominent role of SN II, as in the case of the observed super-Solar [α/Fe] abundances, we note that the [Na/Fe] gradient is somehow steeper than the [α/Fe] gradient. This may indicate an additional role for metallicity, which may have boosted the Na-yields in the central, metal-rich regions of M87.

Finally, thanks to the fine spatial sampling afforded by the quality of our MUSE data we find that the radial profile of all our derived stellar-population properties, i.e. the IMF slope Γ_b, the metallicity [Z/H] and the [α/Fe] and [Na/Fe] abundance ratios, appear to flatten towards the centre of M87, at about the same distance where the surface brightness profile breaks away and starts to fall short from a single Sérsic profile. Interestingly, such a coincidence would be consistent with the currently accepted scenario for the formation of the central surface brightness cores of massive ETGs, following a merger event and the ensuing hardening of a supermassive black hole binary.

Our work adds the case of the massive, central-cluster galaxy M87 to the relatively few objects that as of today have radial constraints on the low-mass end of the IMF, while also illustrating the accuracy that MUSE integral-field observations can bring in this kind of studies (see also, e.g. Mentz et al. 2016). High-quality data are indeed most welcome in this respect since notwithstanding systematic differences in the stellar-population modelling approaches, it already appears that ETGs may present rather different IMF gradients, even when considering objects of similar mass (e.g. the massive objects of van Dokkum et al. 2017 and La Barbera et al. 2017). An exceptional data-quality will be also needed by future dynamical modelling efforts which, similar to the work of Oldham & Auger in M87, may explore the presence of radial variations of the total mass-to-light ratio in ETGs (see also, e.g. Davis & McDermid 2017) and thus provide a way to further test for stellar-population models. In fact, assisted by adaptive optics, it will now be possible to use MUSE to tackle IMF variations down to the nuclear regions of ETGs and of the bulges of spiral galaxies. This may impact on measurements for the mass of central supermassive black holes based on stellar dynamics and help understanding the systematics differences between black hole mass measurements from different tracers of the gravitational potential.

ACKNOWLEDGEMENTS

We wish to thank the anonymous referee for providing valuable comments to this work. MS is indebted to G. Cescutti, K. Gebhardt, C. Kobayashi, S. Viaene, and J. Walsh for their suggestions and to L. Oldham and M. Auger for sharing with us their IMF results prior to the acceptance of their work. MS also acknowledges the hospitality of the European Southern Observatory where part of this work was carried out. CS has received funding from the European Union’s Horizon 2020 research and innovation programme under the Marie Sklodowska-Curie actions grant agreement no. 664931. DK thanks P. Weilbacher for a suggestion to use restricted sky list. This publication has made use of code written by James R. A. Davenport.

REFERENCES

Alton P. D., Smith R. J., Lucey J. R., 2017, MNRAS, 468, 1594
Arrigoni M., Trager S. C., Somerville R. S., Gibson B. K., 2010, MNRAS, 402, 173
Auger M. W., Treu T., Gavazzi R., Bolton A. S., Koopmans L. V. E., Marshall P. J., 2010, ApJ, 721, L163
Bacon R. et al., 2010, in McLean I. S., Ramsay S. K., Takami H., eds, Proc. SPIE Conf. Ser. Vol. 7735, Ground-based and Airborne Instrumentation for Astronomy III. SPIE, Bellingham, p. 773508
Baes M. et al., 2010, A&A, 518, L53
Bastian N., Covey K. R., Meyer M. R., 2010, ARA&A, 48, 339
Bensby T., Feltzing S., Oey M. S., 2014, A&A, 562, A71
Cappellari M., Copin Y., 2003, MNRAS, 342, 345
Cappellari M., Emsellem E., 2004, PASP, 116, 138
Cappellari M. et al., 2011, MNRAS, 413, 813

Downloaded from https://academic.oup.com/mnras/article/478/3/4084/4992755 by Biblioteca di Scienze, Università degli studi di Firenze user on 22 April 2021

Cappellari M. et al., 2012, Nature, 484, 485
Cappellari M. et al., 2013, MNRAS, 432, 1862
Cenarro A. J., Cardiel N., Gorgas J., Peletier R. F., Vazdekis A., Prada F., 2001, MNRAS, 326, 959
Cervantes J. L., Vazdekis A., 2009, MNRAS, 392, 691
Chabrier G., Hennebelle P., Charlot S., 2014, ApJ, 796, 75
Cid Fernandes R., Mateus A., Sodré L., Stasińska G., Gomes J. M., 2005, MNRAS, 358, 363
Conroy C., van Dokkum P., 2012a, ApJ, 747, 69
Conroy C., van Dokkum P. G., 2012b, ApJ, 760, 71
Côté P. et al., 2006, ApJS, 165, 57
Davies R. L., Sadler E. M., Peletier R. F., 1993, MNRAS, 262, 650
Davis T. A., McDermid R. M., 2017, MNRAS, 464, 453
Emsellem E., Krajnović D., Sarzi M., 2014, MNRAS, 445, L79 (EKS14)
Falcón-Barroso J., Sánchez-Blázquez P., Vazdekis A., Ricciardelli E., Cardiel N., Cenarro A. J., Gorgas J., Peletier R. F., 2011, A&A, 532, A95
Ferrarese L. et al., 2006, ApJS, 164, 334
Ferreras I., Weidner C., Vazdekis A., La Barbera F., 2015, MNRAS, 448, 82
Fontanot F., De Lucia G., Hirschmann M., Bruzual G., Charlot S., Zibetti S., 2017, MNRAS, 464, 3812
García-Benito R. et al., 2015, A&A, 576, A135
Gebhardt K., Adams J., Richstone D., Lauer T. R., Faber S. M., Gültekin K., Murphy J., Tremaine S., 2011, ApJ, 729, 119
Girardi L., Bressan A., Bertelli G., Chiosi C., 2000, A&AS, 141, 371
Hopkins P. F., 2013, MNRAS, 430, 1653
Jeong H., Yi S. K., Kyeong J., Sarzi M., Sung E.-C., Oh K., 2013, ApJS, 208, 7
Johansson J., Woods T. E., Gilfanov M., Sarzi M., Chen Y.-M., Oh K., 2014, MNRAS, 442, 1079
Kausch W. et al., 2015, A&A, 576, A78
Kobayashi C., Umeda H., Nomoto K., Tominaga N., Ohkubo T., 2006, ApJ, 653, 1145
Krajnović D. et al., 2015, MNRAS, 452, 2
Krumholz M. R., 2011, ApJ, 743, 110
Kuntschner H. et al., 2010, MNRAS, 408, 97
La Barbera F., Ferreras I., Vazdekis A., de la Rosa I. G., de Carvalho R. R., Trevisan M., Falcón-Barroso J., Ricciardelli E., 2013, MNRAS, 433, 3017 (LB13)
La Barbera F., Ferreras I., Vazdekis A., 2015, MNRAS, 449, L137
La Barbera F., Vazdekis A., Ferreras I., Pasquali A., Cappellari M., Martín-Navarro I., Schönebeck F., Falcón-Barroso J., 2016, MNRAS, 457, 1468
La Barbera F., Vazdekis A., Ferreras I., Pasquali A., Allende Prieto C., Röck B., Aguado D. S., Peletier R. F., 2017, MNRAS, 464, 3597 (LB17)
Leier D., Ferreras I., Saha P., Charlot S., Bruzual G., La Barbera F., 2016, MNRAS, 459, 3677
Loubser S. I., Hoekstra H., Babul A., O'Sullivan E., 2018, MNRAS, 477, 335
Lyubenova M. et al., 2016, MNRAS, 463, 3220
Macchetto F., Pastoriza M., Caon N., Sparks W. B., Giavalisco M., Bender R., Capaccioli M., 1996, A&AS, 120, 463
Macchetto F., Marconi A., Axon D. J., Capetti A., Sparks W., Crane P., 1997, ApJ, 489, 579
Marks M., Kroupa P., Dabringhausen J., Pawlowski M. S., 2012, MNRAS, 422, 2246
Martín-Navarro I., Barbera F. L., Vazdekis A., Falcón-Barroso J., Ferreras I., 2015a, MNRAS, 447, 1033
Martín-Navarro I., La Barbera F., Vazdekis A., Ferré-Mateu A., Trujillo I., Beasley M. A., 2015b, MNRAS, 451, 1081
Martín-Navarro I. et al., 2015c, ApJ, 806, L31
McConnell N. J., Lu J. R., Mann A. W., 2016, ApJ, 821, 39
McDermid R. M. et al., 2014, ApJ, 792, L37
McDermid R. M. et al., 2015, MNRAS, 448, 3484
Mentz J. J. et al., 2016, MNRAS, 463, 2819
Milosavljević M., Merritt D., 2001, ApJ, 563, 34
Nedelchev B., Sarzi M., Kaviraj S., 2017, MNRAS, preprint (arXiv:1705.07994)
Newman A. B., Treu T., Ellis R. S., Sand D. J., Nipoti C., Richard J., Jullo E., 2013, ApJ, 765, 24
Oldham L. J., Auger M. W., 2016, MNRAS, 457, 421
Oldham L., Auger M., 2018, MNRAS, 474, 4169
Padoan P., Nordlund Å., 2002, ApJ, 576, 870
Park J., Jeong H., Yi S. K., 2015, ApJ, 809, 91
Pietrinferni A., Cassisi S., Salaris M., Castelli F., 2004, ApJ, 612, 168
Piontek F., Steinmetz M., 2011, MNRAS, 410, 2625
Pipino A., D'Ercole A., Chiappini C., Matteucci F., 2010, MNRAS, 407, 1347
Ricciardelli E., Vazdekis A., Cenarro A. J., Falcón-Barroso J., 2012, MNRAS, 424, 172
Sánchez S. F. et al., 2012, A&A, 538, A8
Sánchez-Blázquez P. et al., 2006, MNRAS, 371, 703section
Sarzi M. et al., 2006, MNRAS, 366, 1151
Sarzi M., Kaviraj S., Nedelchev B., Tiffany J., Shabala S. S., Deller A. T., Middelberg E., 2016, MNRAS, 456, L25
Scott N. et al., 2009, MNRAS, 398, 1835
Scott N. et al., 2013, MNRAS, 432, 1894
Smette A. et al., 2015, A&A, 576, A77
Smith R. J., Lucey J. R., Carter D., 2012, MNRAS, 426, 2994
Smith R. J., Alton P., Lucey J. R., Conroy C., Carter D., 2015, MNRAS, 454, L71
Sonnenfeld A., Treu T., Gavazzi R., Marshall P. J., Auger M. W., Suyu S. H., Koopmans L. V. E., Bolton A. S., 2012, ApJ, 752, 163
Spiniello C., Trager S. C., Koopmans L. V. E., Chen Y. P., 2012, ApJ, 753, L32
Spiniello C., Trager S., Koopmans L. V. E., Conroy C., 2014, MNRAS, 438, 1483
Spiniello C., Barnabè M., Koopmans L. V. E., Trager S. C., 2015a, MNRAS, 452, L21
Spiniello C., Trager S. C., Koopmans L. V. E., 2015b, ApJ, 803, 87
Thomas D., Maraston C., Bender R., 2003, MNRAS, 339, 897
Thomas D., Maraston C., Bender R., Mendes de Oliveira C., 2005, ApJ, 621, 673
Thomas D., Maraston C., Johansson J., 2011a, MNRAS, 412, 2183
Thomas J. et al., 2011b, MNRAS, 415, 545
Trager S. C., Worthey G., Faber S. M., Burstein D., González J. J., 1998, ApJS, 116, 1
Treu T., Auger M. W., Koopmans L. V. E., Gavazzi R., Marshall P. J., Bolton A. S., 2010, ApJ, 709, 1195
Tsujimoto T., Nomoto K., Yoshii Y., Hashimoto M., Yanagida S., Thielemann F.-K., 1995, MNRAS, 277, 945
Valdes F., Gupta R., Rose J. A., Singh H. P., Bell D. J., 2004, ApJS, 152, 251
van Dokkum P. G., Conroy C., 2010, Nature, 468, 940
van Dokkum P., Conroy C., Villaume A., Brodie J., Romanowsky A. J., 2017, ApJ, 841, 68
Vazdekis A., Casuso E., Peletier R. F., Beckman J. E., 1996, ApJS, 106, 307
Vazdekis A., Cenarro A. J., Gorgas J., Cardiel N., Peletier R. F., 2003, MNRAS, 340, 1317
Vazdekis A., Ricciardelli E., Cenarro A. J., Rivero-González J. G., Díaz-García L. A., Falcón-Barroso J., 2012, MNRAS, 424, 157
Vazdekis A. et al., 2015, MNRAS, 449, 1177
Veale M., Ma C.-P., Greene J. E., Thomas J., Blakeslee J. P., Walsh J. L., Ito J., 2018, MNRAS, 473, 5446
Ventura P., Di Criscienzo M., Carini R., D'Antona F., 2013, MNRAS, 431, 3642
Walsh J. L., Barth A. J., Ho L. C., Sarzi M., 2013, ApJ, 770, 86
Weidner C., Ferreras I., Vazdekis A., La Barbera F., 2013, MNRAS, 435, 2274
Zieleniewski S., Houghton R. C. W., Thatte N., Davies R. L., 2015, MNRAS, 452, 597

Downloaded from https://academic.oup.com/mnras/article/478/3/4084/4992755 by Biblioteca di Scienze, Università degli studi di Firenze user on 22 April 2021

APPENDIX A: SURFACE BRIGHTNESS AND VELOCITY DISPERSION PROFILE OF M87

To help interpreting Figs 9 and 10 here we further show in Fig. A1 the surface brightness and velocity dispersion profiles of M87 as measured with the MUSE data. This is in particular to point to the onset of the central core in the surface brightness profile and to how the stellar velocity dispersion profile reaches a plateau at around 20 arcsec from the centre, where the latter behaviour contrasts to the case of all our line-strength and stellar-population property measurements that all show a monotonically decreasing profile. Interestingly, the stellar velocity dispersion appears even to show a positive gradient in the outskirt of M87, similar to other massive and central cluster galaxies (Newman et al. 2013; Loubser et al. 2018; Veale et al. 2018).

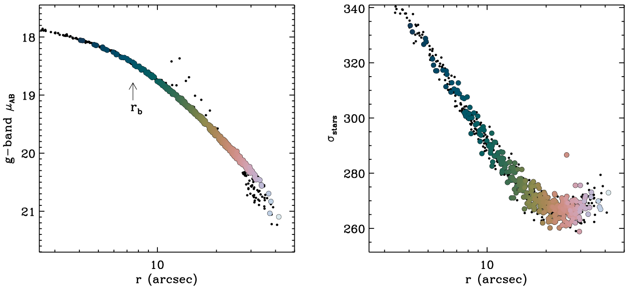

Figure A1. Stellar *g*-band surface brightness (left) and velocity dispersion (right) of M87 as measured through the MUSE data. Radial limits and coloured points are as in Fig. 9, whereas the small black dots correspond to the Voronoi bins that have been excluded from our stellar-population analysis (see Sections 3.3 and 3.4). As in Fig. 9 in the vertical arrow in the left-hand panel indicate the break radius r_b where the surface brightness flattens and departs from a single Sérsic profile.

This paper has been typeset from a TEX/LATEX file prepared by the author.

Downloaded from https://academic.oup.com/mnras/article/478/3/4084/4992755 by Biblioteca di Scienze, Università degli studi di Firenze user on 22 April 2021